Dual human lung models reveal compartment-specific activity of anti-tuberculosis drugs and host-directed therapies

Caio César Barbosa Bomfim[1*†], Natacha Faivre[1,2*], Thomas Benoist[1], Manon Popis[1], Bastien Suire[1], David Pericat[1], José Manuel Sánchez-López[1,3,4], Beatriz Melissa Aponte-Castillo[3], Emmanuelle Näser[1], Pénélope Viana[1], Nicolas Guibert[5], Romain Vergé[1,6], Julien Mazières[5], Arnaud Métais[1], Renaud Poincloux[1], Brigitte Raynaud-Messina[1], Fabrice Dumas[1], Olivier Neyrolles[1,2], Christel Vérollet[1,2], Etienne Meunier[1], Geanncarlo Lugo-Villarino[1,2#] and Céline Cougoule[1#†]

[1] Institut de Pharmacologie et de Biologie Structurale (IPBS), Université de Toulouse, CNRS, Toulouse, France

[2] International Research Project CNRS "MAC-TB/HIV", Toulouse, France, and Buenos Aires, Argentina

[3] Unidad de Investigación Médica en Genética Humana (UIMGH), Hospital de Pediatría Centro Médico Nacional Siglo XXI, Instituto Mexicano del Seguro Social (IMSS), México

[4] Children's Hospital of Tlaxcala, Tlaxcala, 90610, México

[5] Service de Pneumologie, Hôpital Larrey, CHU de Toulouse, Toulouse, France

[6] Service de Chirurgie Thoracique, Hôpital Larrey, CHU de Toulouse, Toulouse, France

*These authors contributed equally to this work

[#] These senior authors contributed equally to this work

[†]Correspondence: Caio Bomfim (Caio.Bomfim@ipbs.fr); Céline Cougoule (Celine.Cougoule@ipbs.fr)

Keywords: *Mycobacterium tuberculosis*, Alveolar macrophages, Air–liquid interface cultures, Host-directed therapy, Antibiotics, Antimicrobial efficacy

Running title: Drug Efficacy and Host Response in Human Lung Models

SUMMARY

Tuberculosis (TB) remains a major global health challenge that requires new therapeutic strategies to improve drug efficacy, shorten treatment duration, prevent drug resistance, and limit *Mycobacterium tuberculosis* (Mtb) persistence. Here, we established complementary *in vitro* human lung models integrating alveolar macrophage-like (AML) cells and airway air-liquid interface (ALI) cultures to evaluate standard-of-care antibiotics, host-directed therapies, and virulence-targeting agents. AMLs recapitulated key morphological, transcriptional, and functional features of primary alveolar macrophages, including a $CD16^+$ immunoregulatory phenotype highly permissive to Mtb infection. In parallel, ALI cultures maintained epithelial barrier integrity and secretory functions, allowing apical Mtb infection, drug penetration analysis, and inflammatory profiling. Benchmarking of standard-of-care antibiotics revealed compartment-specific activity: isoniazid, rifampicin, and moxifloxacin were effective in both systems, while pyrazinamide was active only in AMLs. Anti-inflammatory host-directed therapies such as ibuprofen and doramapimod selectively reduced cytokine production without affecting bacterial load. Together, this dual-platform system offers a physiologically relevant and scalable model to assess antimicrobial efficacy and host modulation across distinct pulmonary niches, bridging the gap between conventional macrophage assays and the complex human lung.

1. INTRODUCTION

Tuberculosis (TB) remains a major global public health challenge, affecting millions of people every year. Caused by *Mycobacterium tuberculosis* (Mtb), it accounts for over 10 million new infections annually and continues to be the leading cause of death from a single agent, claiming approximately 1.25 million lives lost in 2023 alone (1). Although several effective antibiotic regimens exist, TB still shows a high relapse rate, with treatment success achieved in about 88% of patients with drug-sensitive TB (1, 2). Standard treatment for drug-sensitive TB lasts approximately six months. However, the prolonged duration of therapy often leads to poor patient adherence, contributing to relapse and the emergence of drug resistance. In cases of rifampicin-resistant or multidrug-resistant TB, treatment regimens are even longer, lasting up to 24 months, and are associated with lower treatment success rates (approximately 68%), further exacerbating the global disease burden. Together, these challenges underscore the urgent need for new and more effective treatment options.

Mtb has adapted to evade the host immune response, especially by interfering with macrophage microbicidal functions. These mononuclear phagocytes play a unique role in TB, serving as both the primary reservoir for Mtb replication and the key effector cells that control the infection. This dual function is central to the outcome of TB disease. Importantly, although many individuals encounter the bacteria, only about 5% to 10% develop active TB (3), which highlights the effectiveness of innate and adaptive immune responses in conferring host resistance (4). This has sparked interest in therapeutic strategies that target the interaction between immune cells and Mtb. By boosting macrophage ability to fight bacteria or countering the immune suppression caused by Mtb, for example, these so-called host-directed therapies (HDTs) may enhance the effectiveness of antibiotics. Consequently, this may lead to shorter treatment times, lower relapse rates, and help prevent the emergence of MDR Mtb strains.

Recent research reveals that a macrophage's origin and its specific tissular niche shape its phenotypic and functional characteristics (5). The lung niche comprises unique local signals, such as growth factors and metabolic cues, as well as interactions with surrounding tissue components. Understanding these dynamics is particularly important in the TB context, as ontogeny and the specific lung niche influence how macrophages respond to and control Mtb (6, 7). Therefore, for therapeutic approaches targeting the interaction between macrophages and Mtb to be effective, it is essential to consider both their origin and the specific lung niche in which they reside.

Mtb primarily infects alveolar macrophages (AMs) upon initial lung invasion, exploiting their supportive metabolic environment and immune tolerance (6, 8). These macrophages are long-lived

78 and self-renewing, mainly originating from the yolk sac and fetal liver during development. They are
79 replenished by blood circulating monocytes derived from the bone marrow, particularly in older
80 individuals or following an inflammatory insult such as an infection (5, 9). Within the alveolar niche,
81 AMs reside in elevated oxygen levels and lipid-rich surfactant, as well as in signals from airway
82 epithelial-derived cytokines, such as granulocyte-macrophage colony-stimulating factor (GM-CSF)
83 and transforming growth factor-β (TGF-β) (10). These environmental signals promote a tolerogenic
84 phenotype in AMs by inhibiting the activation of pro-inflammatory pathways, which is essential for
85 maintaining pulmonary homeostasis and preventing unnecessary inflammation against inert or non-
86 pathogenic particles. However, this also creates an intracellular environment that is permissive to
87 bacterial replication (6, 7, 11). Understanding the interplay between AMs and Mtb is crucial for
88 proposing novel therapies that direct the host response.

89 As of today, most *in vitro* studies evaluating anti-TB drugs rely on macrophage cell lines, such
90 as the human THP-1–based cellular models, or on M-CSF-driven human blood monocyte-derived
91 macrophages (MDMs) (12–14). Yet, these models do not fully recapitulate the characteristics and
92 functions of AMs, nor do they adequately represent the alveolar niche. Recent developments have
93 introduced novel human AM models generated *in vitro* from pluripotent stem cells (15, 16) or from
94 peripheral blood monocytes (17, 18), which offer greater experimental tractability. In particular, the
95 AM-like (AML) model adapted by Pahari and colleagues, using human monocytes differentiated with
96 a specific combination of GM-CSF, TGF-β, interleukin 10 (IL-10), and surfactant, closely resembles
97 primary AMs in terms of phenotype, metabolic activity, and functions. This model shows increased
98 expression of peroxisome proliferator-activated receptor gamma (PPAR-γ) and greater susceptibility
99 to intracellular Mtb proliferation compared to traditional MDMs (18). Likewise, recent advances in
100 air–liquid interface (ALI) cultures derived from human bronchial epithelial cells (HBECs) provide key
101 structural and functional features of the airway epithelium, delivering better reproducibility and
102 suitability for medium- and high-throughput applications (19–21). Notably, these ALI cultures
103 enable infection via apical inoculation of Mtb, mimicking the natural infection route, which leads to
104 a fully developed infection and relevant physiological responses (22, 23). Nonetheless, the extent
105 to which these *in vitro* approaches can reliably predict *in vivo* outcomes in human TB, particularly
106 concerning host-targeted therapies, remains largely unexplored.

107 To address this, the present study established a dual *in vitro* system comprising the AML
108 model and airway ALI cultures. This system recapitulates the two main lung compartments engaged
109 by Mtb: the intracellular AM niche, considered to be permissive for bacterial growth, and the airway
110 barrier, which both restricts pathogen invasion and drives inflammation. This combined approach

enables the systematic evaluation of anti-TB compound testing, benchmarking their performance against molecules representing distinct pharmacological classes, including standard-of-care antibiotics, host-directed therapies, and virulence-targeting therapies. In this manner, this dual *in vitro* system aligns with the growing priority of co-targeting Mtb and the host to overcome therapeutic limitations.

116 **2.** METHODS

117 2.1 Bacterial Culture

118 The genetically modified H37Rv-GFP and H37Rv-dsRED strains were grown in Middlebrook 7H9
119 medium supplemented with 0.05% Tween 80 (Euromedex) and 10% ADC (albumin, dextrose, and
120 catalase, BD). The strain H37Rv::lux was constructed after transformation of the Mtb wild type
121 strain H37Rv with the integrative plasmid pMV30-hsp-Lux13 (Addgene #26161) and cultivated
122 with the same medium described before, plus kanamycin (50 µg/mL). Both bacterial strains were
123 maintained in culture at 37°C until the mid-log phase (OD 0.6–0.9) on day 7.

124

125 2.2 Drugs

126 The benchmarking compounds used in this study were kindly provided by GSK Global Health
127 Medicines R&D, including standard-of-care antibiotics, host-directed therapies, and virulence-
128 targeting therapies. The identity, mechanism of action, and therapeutic class of each drug are
129 summarized in Table S1, which provides annotated information relevant to TB control.

130

131 2.3 AML and MDM Generation, Infection, and Treatment

132 Human primary monocytes were isolated from the healthy subject's buffy coat (provided by
133 Etablissement Français du Sang, Toulouse, France, under contract 21RB2025-028-R and
134 21RB2025-031-R). According to articles L12434 and R124361 of the French Public Health Code,
135 the contract was approved by the French Ministry of Science and Technology (agreement number
136 AC 2009921). Written informed consents were obtained from the donors before sample
137 collection. Monocytes ($CD14^+$) were isolated from peripheral blood cells using magnetic positive
138 selection (Miltenyi Biotec). For differentiation into MDM, the $CD14^+$ monocytes were cultivated
139 in a 24-well plate (0.5×10^6 cells/well) for seven days in RPMI-1640 Glutamax (Gibco), 10% Fetal
140 Bovine Serum (FBS, Sigma-Aldrich), and human M-CSF (20 ng/mL, Miltenyi), as previously
141 described (24).

142 For differentiation into AML, the $CD14^+$ monocytes were cultivated in a 24-well plate ultra-low
143 attachment (2×10^6 cells/well) for 6–7 days with RPMI-1640 Glutamax medium supplemented
144 with 10% FBS, 1% penicillin-streptomycin (Gibco), and IL-10 (5 ng/mL, Miltenyi Biotec), TGF-β (5
145 ng/mL, Miltenyi Biotec), and GM-CSF (10 ng/mL, Miltenyi Biotec), as well as Curosurf (100 µg/mL,
146 Chiesi) (17, 18). The medium was refreshed every 2–3 days. After differentiation, the AMLs were
147 infected with the H37Rv-GFP, H37Rv-DsRED or H37Rv::lux Mtb strain (MOI indicated in the
148 related figures) for 3 hours or overnight (TEM experiment), washed three times with PBS and

149 then they were plated ($2x10^5$ cells/well) in a 96-well plate ultra-low-attachment, treated with
150 different compounds (concentrations indicated in the related figures) and incubated at 37°C, 5%
151 CO_2 during six days.
152
153 2.4 Broncho-Alveolar Lavage from Patients
154 Broncho-alveolar lavage was performed using a flexible bronchoscope inserted through the nose
155 with local anesthesia. The lavage samples were processed as outlined by (25), and the cells were
156 stained for flow cytometry analysis. Patient samples were obtained through a contract between
157 IPBS/CNRS and Toulouse hospital (reference 257619, April 19th, 2022), after informed consent,
158 in accordance with the Declaration of Helsinki. Clinical and biological annotations of the samples
159 have been declared to the CNIL ("Comité National Informatique et Libertés").
160
161 2.5 Airway Organoids
162 The organoids were derived from tumor-adjacent normal lung tissue obtained from patients with
163 lung cancer undergoing surgical resection, as previously described (26, 27). Briefly, the tissue was
164 dissociated into single cells and cultured in an extracellular matrix (Cultrex Basement Membrane
165 Extract, Type 2, R&D Systems) with culture medium supplemented with various growth factors
166 and inhibitors for four weeks, as originally described (27). The medium was refreshed every 3–4
167 days.
168
169 2.6 Air-Liquid Interface (ALI) Culture, Infection, and Treatment
170 Airway organoids were dissociated and seeded onto transwell plate inserts as previously
171 described (28). The cultures were incubated submerged in PneumaCult Ex-Plus medium
172 (StemCell Technologies) until reaching confluency. Once confluent, PneumaCult ALI medium
173 (StemCell Technologies) was added exclusively to the basal side, leaving the apical side exposed
174 to air (ALI). The cultures were then maintained at ALI conditions for an additional three weeks,
175 with the medium refreshed every 2–3 days. For infection, Mtb ($4x10^5$ bacilli in 20 µL per well)
176 was added to the apical side of the ALI culture, with treatment administered in the basal medium.
177 Cultures were incubated at 37°C for six days, with medium and treatment refreshed on day 3.
178
179 2.7 Cytokine Quantification
180 After six days of infection, the AMLs were centrifuged, and the supernatants were collected for
181 analysis of cytokine production using Lumit immunoassay kits (Promega). For the ALI cultures,

182 the medium from the basal side was harvested on days 3 and 6 post-infection, and cytokine levels
183 were quantified by ELISA (Invitrogen).
184
185 2.8 Bacterial Load Measurement
186 To quantify bacterial load by colony-forming unit (CFU) assay, the samples were lysed with 0.1%
187 Triton X-100 (Euromedex) in water. Serial dilutions were prepared and plated on 7H11 agar
188 medium supplemented with OADC. Colony counts were performed after 23 days of incubation
189 at 37 °C. In experiments where AMLs were infected with the H37Rv-GFP strain, the samples were
190 fixed with PFA 4%, and bacterial load was assessed by measuring GFP fluorescence intensity using
191 spectral flow cytometry (Northern Lights, Cytek). In experiments with AMLs infected with the
192 H37Rv::lux strain, bacterial load was directly measured as relative light units (RLU) using the
193 GlowMax luminometer (Promega). For ALI cultures, the tissue was lysed by adding 200 µL of lysis
194 buffer (0.1% Triton X-100) to the inserts. The lysate was then collected, and the luminescence
195 was measured using the GlowMax luminometer.
196
197 2.9 Measurement of Gene Expression by RT-PCR
198 AML and MDM cell pellets were homogenized with 350 µl of RNA extraction buffer (RLT lysis
199 buffer, Qiagen) by pipetting ten times, then briefly centrifuged at 2000g for 5 seconds.
200 Homogenized cell lysates were then conserved at -80°C. RNA was extracted from cell lysates
201 using a Qiagen RNeasy Mini Kit according to the manufacturer's instructions. RNA quality was
202 assessed with the two measuring absorbance ratios Absλ = 260 nm/Absλ = 280 nm and
203 Absλ = 260 nm/Absλ = 230 nm using a Thermofisher Nanodrop. The RNA was then stored at -
204 80°C. For each sample, a fixed quantity (150-250ng) of extracted mRNA was reverse-transcribed
205 into cDNA by mixing 1 µl of it with Reverse Transcriptase, deoxynucleotide triphosphates
206 (dNTPs), oligo dTs, reverse transcription (RT) buffer solutions, and RNase-free water (for a 20 µl
207 reaction), as part of the Verso cDNA Synthesis Kit. cDNA was stored at -20°C. A no reverse
208 transcriptase control was also performed to test for remaining contaminating genomic DNA in
209 the extracted RNA. The mixes were then heated in a Nexus GX2 Mastercycler thermocycler for
210 the reaction to occur (30 min at 42°C and 2 min at 90°C). Finally, cDNA was mixed with Forward
211 and Reverse primers for the genes of interest, along with SYBR Green Master Mix, in technical
212 triplicate in a 96-well plate, and then subjected to RT-qPCR. Plates were loaded into a 7500 Real-
213 Time PCR System thermocycler, which proceeded as follows: 50°C for 2 min, then 95°C for 10

214 min, then 40 cycles of 95°C for 15 sec and 60°C for 1 min. The primer sequences used for this
215 analysis are listed in the Supplementary Material (Table 2).
216
217
218 2.10 Western Blot
219 Cell lysates were homogenized by adding 1X final Laemmli Sample Buffer (BIO-RAD) (95 °C) and
220 pipetting up and down ten times. Next, the samples were heated at 95°C for five minutes and
221 stored at -20°C. 20 µl of sample and PageRuler Prestrained Protein Ladder (ThermoFisher) were
222 loaded onto 10% acrylamide gels, migrated at 120V for one hour, and then transferred onto
223 polyvinylidene fluoride (PVDF) membranes. After transfer, the membrane was saturated for one
224 hour at room temperature in TBS-T (Tris 10 mM, pH 8, NaCl 150 mM, Tween 20 at 0.05%)
225 containing 5% Bovine Serum Albumine (BSA, Euromedex). Then, the membrane was incubated
226 overnight at 4°C with the primary antibody, under agitation. After three 10-minute washes with
227 TBS-T, the membrane was incubated with the secondary antibody conjugated to the horseradish
228 peroxidase enzyme (HRP) for one hour at room temperature under agitation. Then, the
229 membranes were washed three times for 20 min with TBS-T. The membranes were revealed
230 using the WesternBright Quantum Western blotting revelation kit (ThermoFisher), and a
231 WesternSure Pen (Licorbio) was used for the scale ladder. Images were acquired using the C-
232 DiGit Blot Scanner (Licorbio). The primary and secondary antibodies are listed in the
233 Supplementary Material (Table 3). Membranes could then be incubated in Antibody Stripping
234 Buffer (1x) (Euromedex) for 5 min and washed 3-5 times in T-BST, then distilled to be reused for
235 staining.
236
237 2.11 Spectral Flow Cytometry
238 After infection at the indicated times, the culture medium was discarded, and Mtb-infected cells
239 were collected as previously described (24). Cells were then incubated with Human TruStain FcX
240 (Biolegend) in a staining buffer (PBS, 1% FBS) for 10 min and labeled using ViaDye Red (Cytek,
241 1:2000) in PBS (Gibco) at room temperature for 20 min. Then, cell surface proteins were stained
242 for 20 min in a staining buffer containing True-Stain Monocyte Blocker (Biolegend) at 4°C. The
243 fluorescent antibodies are listed in the Supplementary Material (Table 4). Cells were then fixed
244 with 3.7% paraformaldehyde (PFA; EMS, DeltaMicroscopies) for two hours and then resuspended
245 in staining buffer. The samples were acquired using spectral flow cytometry with a Northern
246 Lights (Cytek) instrument and analyzed with SpectroFlo V3.3.0 Software to subtract

247 autofluorescence, followed by analysis with FlowJo V10 Software. The samples were cleaned and
248 standardized using PeacoQC and the Mutual Nearest Neighbour method, respectively. For
249 unbiased analysis, we used t-SNE on the concatenated sample (including all control and infected
250 samples). Within the t-SNE map, a gate was created for the control group and another gate for
251 the infected group.
252
253
254 2.12 Scanning Electron Microscopy (SEM)
255 ALI culture was infected with H37Rv::lux (MOI 2:1) as described above. After six days, the culture
256 medium was discarded, and cells were fixed with 3.7% PFA in PBS for two hours. ALI were further
257 fixed using 0.1 M sodium cacodylate buffer (pH 7.4) supplemented with 2.5% (vol/vol)
258 glutaraldehyde (Euromedex). Then, they were washed three times for 5 min in 0.2 M cacodylate
259 buffer (pH 7.4), post-fixed for 1 hour in 1% (wt/vol) osmium tetroxide in 0.2 M cacodylate buffer
260 (pH 7.4), and washed with distilled water. Samples were dehydrated through a graded ethanol
261 series (25–100%), transferred to acetone, and critical-point dried with CO_2 in a Leica EM CPD300.
262 Dried specimens were sputter-coated with 3 nm of platinum using a Leica EM MED020
263 evaporator and were examined with a FEI Quanta FEG250.
264
265 2.13 Transmission Electron Microscopy (TEM)
266 AMLs were infected with Mtb-dsRED (overnight, MOI 2), as described above. After 24 hours, the
267 culture medium was discarded, and the cells were fixed using 3.7% PFA and 30 mM sucrose in
268 PBS for 2 hours. The cells were fixed in 2.5% glutaraldehyde and 2% PFA dissolved in 0.1 M
269 Sorensen phosphate buffer (pH 7.2) (DeltaMicroscopies) for 2 hours at room temperature, and
270 then preserved in 1% PFA dissolved in 0.1M Sorensen's phosphate buffer. Adherent cells were
271 treated for one hour with 1% aqueous uranyl acetate, then dehydrated in a graded ethanol series
272 and embedded in Epon. Sections were cut on a Leica Ultracut microtome, and ultrathin sections
273 were mounted on 200-mesh Formvar-coated carbon-coated copper grids. Finally, thin sections
274 were stained with 1% uranyl acetate and lead citrate and examined using a transmission electron
275 microscope (Jeol JEM-1400) at an accelerating voltage of 80 kV. Images were acquired using a
276 digital camera (Gatan Orius) and colorized with the Photoshop software (Adobe).
277
278
279

280 2.14 Histological staining

281 ALI cultures were fixed for 48 hours in 10 % neutral-buffered formalin (Sigma), rinsed thoroughly,
282 and resuspended in Hank's Balanced Salt Solution (HBSS, Gibco), and then stored at 4 °C until
283 further processing. After being embedded in paraffin, the sections (5 µm) were stained with
284 hematoxylin (BioGnost HEMML-OT-100) and eosin Y (Sigma). The cells were stained with Alcian
285 blue 8GX (Fluka 66011-500ml-F) for 30 min, washed in tap water for 2 min, and counterstained
286 with nuclear fast red (Sigma) for 5 min. Images were acquired using a Zeiss Axio Imager M2 using
287 either a 10x/0.3 EC Plan-Neofluar or 20x/0.8 Plan Apochromat Zeiss objective, and using a Zeiss
288 Axiocam 503 color camera. Images were processed using the Zeiss Zen software.

289 2.15 Bioinformatic Analysis

290 For the bioinformatic analysis, two different transcriptome datasets were used. Counts and TPM
291 (transcripts per million) matrices were obtained from the NCBI GEO (Gene Expression Omnibus)
292 platform using the accession numbers GSE188945 and GSE189996. The transcriptome profiles
293 were then compared in two scenarios: MDM versus AML and Mtb-infected AM at 72 hours versus
294 uninfected AM. The counts matrix was used to perform the differential expression analysis (DEG)
295 with the DESeq2 algorithm. The false discovery rate (FDR) was managed using the Benjamini-
296 Hochberg method. Genes with an FDR-adjusted p-value of less than 0.05 and an LFC greater than
297 1.5 or less than -1.5 were deemed differentially expressed (29). Gene ontology (GO) terms and
298 biological processes (BP) that were overrepresented were identified using the ClusterProfiler
299 package, relying on a fold discovery rank below 0.05 and an enrichment value of 1 (30). The TPM
300 matrix was utilized for data visualization. Box plots, volcano plots, and heatmaps were generated
301 for the most representative genes of interest. All analyses and visualizations were performed
302 using the R programming language (version 4.5.1) and RStudio, with the help of the ggplot2,
303 DESeq2, and ComplexHeatmap packages.

304

305 2.16 Statistical Analysis

306 Graphs and statistical analyses were performed using Prism software (version 10.5 GraphPad).
307 Non-parametric tests were applied, with paired Wilcoxon or unpaired Mann–Whitney tests used
308 as indicated in each figure legend. Statistical significance was defined as *a P value of* ≤ 0.05. Data
309 are presented as mean ± SD.

310 **3.** RESULTS

311 **Molecular Profiling and Phenotypic Characterization of the Human Alveolar Macrophage-Like Cell**
312 **Model.**

313 To dissect the unique interactions between Mtb and AMs in the pulmonary
314 microenvironment (Fig. 1A, left), we used the recently described human monocyte-derived AML
315 model, which recapitulates key features of primary human AMs (hAM) (11, 17, 18, 31). Briefly,
316 human monocytes were differentiated for 6 days with a combination of GM-CSF, TGF-β, IL-10, and
317 surfactant to obtain AMLs (Fig. 1A, right). First, we confirmed the phenotype of these AMLs by
318 comparing them with MDMs. Consistent with previous studies (17, 18), AMLs exhibited higher gene
319 expression typical of primary hAMs like *MRC1* (CD206), *MARCO*, *CXCL3*, *DUSP1*, *PPARG* (PPAR-γ) and
320 *SPI1* (PU.1), relative to MDMs from the same donor (Supplementary Fig. 1A). In contrast, MDMs
321 expressed significantly higher levels of *MMP7* and *MMP9* compared to AMLs (Supplementary Fig.
322 1A). At the protein level, AMLs showed higher PPAR-γ expression compared to MDMs
323 (Supplementary Fig. 1B), supporting the notion that this AML cell model relies on this transcription
324 factor for its development and functions, as primary hAMs do (17, 18).

325 To determine whether AMLs resemble primary hAMs, we compared surface marker
326 expression in hAMs isolated from bronchoalveolar lavage (BAL) samples of patients with various
327 lung pathologies with AMLs. The majority of hAMs recovered from BAL consisted of a $CD206^{+}CD64^{+}$
328 cell population, within which most cells also expressed CD14 and CD16 (Fig. 1B and Supplementary
329 Fig. 1C). These results are consistent with the literature, which reports high expression of these
330 markers in hAM (32–34). Interestingly, AMLs exhibited a similar phenotype, characterized by a high
331 frequency of $CD206^{+}CD64^{+}$ macrophages, predominantly $CD14^{+}CD16^{+}$ within this gated population
332 (Fig. 1B). Further analysis with a broader panel of cell-surface markers revealed that AMLs closely
333 resemble the phenotype of hAMs. Various key markers, including PD-L1, CD86, CD163, MERTK,
334 MARCO, CXCR4, and CD169, showed similar expression patterns between the two cell types,
335 reinforcing AMLs as a physiologically relevant *in vitro* model for primary hAMs (Fig. 1C).

336 To complement this phenotypic characterization of AMLs, we leveraged a publicly available
337 transcriptomic dataset comparing AML cell model with hAMs and MDMs (17, 18). For this dataset,
338 we extracted a curated panel of genes, including those identified through our phenotypic analysis
339 and reflecting macrophage polarization, lipid metabolism, scavenger receptor activity, matrix
340 remodeling, cytokine production, and immune checkpoint regulation. Consistent with our *in vitro*
341 phenotyping, AMLs displayed a transcriptional profile more closely aligned with anti-inflammatory
342 and tissue-resident markers, including high expression of cell-surface marker genes, such as *FCGR1A*

343 (CD64), *FCGR3A* (CD16), *CD163*, *MRC1* (CD206) and *MARCO*, and the transcription factors *PPARG*
344 (PPAR-γ), similar to hAMs from healthy donors (Supplementary Fig. 2A). These results are reinforced
345 by a tendency toward a higher expression of *SIGLEC1* (CD169) and *CXCR4* in AMLs. In contrast,
346 MDMs showed a marked increase in the matrix-remodeling–related gene *MMP9*, along with a trend
347 toward higher expression of pro-inflammatory markers, including *TNF*, *CD86*, *CD38*, *CCR5*, *CD4*, and
348 *FCAR*. Taken together, these results are consistent with MDM activation toward a more
349 inflammatory, monocyte-derived state (Supplementary Fig. 2A).

350 Beyond the predefined macrophage gene signature, we identified the top genes significantly
351 enriched in AMLs compared with MDMs. The resulting volcano plot revealed a clear separation
352 between these cell populations, as previously reported (17, 18). Among the most highly upregulated
353 genes in AMLs, several have documented roles in immune regulation, tissue remodeling, and
354 metabolism (Supplementary Fig. 2B). Notably, *ABHD5*, a lipase co-activator, has been shown to
355 suppress NF-κB-dependent MMP expression (35), suggesting a potential link to the lower
356 *MMP7*/*MMP9* levels observed in AMLs. *AOC3*, an adhesion molecule and amine oxidase, transiently
357 contributes to adaptive immune responses in the airways (36), aligning with AMLs' lung-shaped
358 phenotype. The complement pathway component *C8B* was also elevated, suggesting enhanced
359 opsonization potential in these cells. *ITIH5*, a member of the inter-alpha-trypsin inhibitor family with
360 reported pro-fibrotic functions (37), and *CHDH*, a mitochondrial choline dehydrogenase regulating
361 mitophagy via *SQSTM1*/*LC3* recruitment (38), were among the other highly expressed transcripts.
362 Interestingly, *CES1*, a carboxylesterase whose inactivation augments lung inflammation in mice (39),
363 and *RBP4*, a retinol-binding protein that primes the NLRP3 inflammasome through TLR2/TLR4
364 signaling (40), point toward potential links between AML lipid metabolism and inflammasome
365 activation. Finally, transcription factor *KLF4*, known to integrate STAT6-dependent alternative
366 activation pathways (41), was prominently upregulated, further supporting the tissue-resident, M2-
367 skewed features of AMLs. Conversely, several genes were markedly downregulated in AMLs
368 compared to MDMs. Among them, *GALM*, a galactose mutarotase involved in glucose metabolism,
369 and *TRAF1*, a TNF receptor–associated factor with established roles in NF-κB signaling and
370 inflammasome activation (42), may reflect metabolic and inflammatory programming differences
371 between the two macrophage populations (Supplementary Fig. 2B). Finally, Gene Ontology (GO)
372 enrichment analysis of AML-upregulated genes highlighted biological processes consistent with
373 their lung-adapted phenotype, including G protein–coupled receptor signaling, response to
374 bacterium, blood vessel development, epithelial cell differentiation, regulation of inflammatory
375 response, lipid homeostasis, and humoral immune response (Supplementary Fig. 2C). These

376 pathways further emphasize the specialized, tissue-resident programming of AMLs, which
377 integrates metabolic adaptation, immune regulation, and barrier-associated functions.
378 Collectively, the AML model closely resembles the morphology, surface markers, and
379 transcriptional profiles of primary hAMs, and differs from those of MDMs. AMLs exhibit tissue-
380 resident, anti-inflammatory, and lipid metabolic signatures, with reduced expression of matrix
381 remodeling and pro-inflammatory genes. These characteristics align with the functions of the
382 alveolar niche, establishing AMLs as a relevant and manageable surrogate for hAMs.
383
384 **Mtb Infection Reveals Phenotypic Heterogeneity and Distinct Activation States in the human**
385 **Alveolar Macrophage-Like Cell model.**
386 To assess whether phagocytic function is preserved after differentiation into AML, we
387 exposed AMLs to Mtb H37Rv expressing GFP. Cells were examined by epifluorescence and light
388 microscopy, as well as transmission electron microscopy (TEM), confirming the presence of Mtb
389 bacilli within intracellular compartments (Supplementary Fig. 3A and Fig. 2A, pink). Of note, TEM
390 analysis revealed AMLs as rounded to oval in shape, featuring irregular plasma membranes that
391 extend into short pseudopodia, a cytoplasm containing many vacuoles and lipid bodies (possible
392 signs of surfactant clearance), numerous electron-dense lysosomes and phagolysosomes (indicative
393 of a possible robust phagocytic activity), mitochondria and smooth endoplasmic reticulum, and a
394 large nucleus, slightly off-center, with a distinct nucleolus (Fig. 2A). While flow cytometry analysis
395 six days post-infection revealed a dramatic increase in cell death at an MOI of 5:1; the MOI of 1:1
396 yielded an intact cell viability with approximately 50% of infected cells (Supplementary Fig. 3B-C).
397 As expected, quantification of bacterial burden over time using different strains and methods
398 (H37Rv::lux for luminescence and H37Rv-GFP for FACS, and both for CFU) showed that Mtb
399 replicates within AMLs (Supplementary Fig. 3D).
400 We next examined the gene expression of AML following infection with Mtb H37Rv-GFP.
401 Notably, we observed a significant reduction of *PPARG* and an increase of *MMP7* and *MMP9*, as well
402 as *TNF*, indicating a transcriptional reprogramming toward an inflammatory response and matrix-
403 degrading phenotype in AML (Fig. 2B). To further characterize the impact of infection, we examined
404 the phenotypic profile of AMLs following infection with Mtb H37Rv-GFP. This analysis showed a
405 marked expansion of the $CD14^{+}CD16^{-}$ subset (Fig. 2C). Analysis of GFP expression revealed that the
406 $CD14^{+}CD16^{+}$ AML subset was significantly more permissive to Mtb infection than its $CD14^{+}CD16^{-}$
407 counterpart (Fig. 2D). We reasoned that these differences in susceptibility could reflect distinct
408 phenotypic programs. To explore this, we next performed a high-dimensional t-SNE analysis on

409 Northern Light spectral flow cytometry data incorporating CD45$^+$ AMLs from infected and
410 uninfected conditions (Fig. 2E). To this end, samples were concatenated and embedded based on
411 the expression of markers associated with proinflammatory activation (*i.e.,* CD86, CD38, CD64) and
412 inflammatory checkpoints (*i.e.,* PD-L1, which, although immunoinhibitory, is strongly induced by
413 inflammatory stimuli). We also included key regulatory and anti-inflammatory molecules (*i.e.,*
414 CD163, CD206, MERTK, MARCO), lipid metabolism, and scavenger receptors (*i.e.,* ABCA1, CD36).
415 This strategy enabled us to resolve infection-driven shifts in activation states and to provide a
416 framework for linking infection status with functional phenotypes. Using this approach, AMLs were
417 separated into control and infected populations, and within each group, we further stratified
418 subsets based on CD16 expression (Fig. 2E). Comparative analysis of surface marker expression
419 among these groups revealed various notable differences. As expected, PD-L1 was substantially
420 upregulated in both CD16$^+$- and CD16$^-$-infected cells compared to uninfected controls. MERTK,
421 CD169, CCR5, CD163, and CD38 expression was increased explicitly in infected cells independently
422 of CD16 expression. Notably, we observed reduced levels of ABCA1 in CD16$^-$ uninfected and Mtb-
423 infected cells. Moreover, we showed that the CD16$^+$ subset, independently of the infection, is
424 characterized by a reduction of the pro-inflammatory marker CD86 and an increase of CD209
425 compared to the CD16$^-$ counterpart (Fig. 2E). Together, these findings indicate that CD16$^+$ and CD16$^-$
426 AMLs adopt distinct activation states in response to Mtb, which may underlie their differential
427 susceptibility to infection.

428 To further characterize these subsets, supervised flow cytometry analysis revealed that
429 under uninfected conditions CD14$^+$CD16$^+$ cells expressed higher levels of CD163, CD169, CD209, and
430 MARCO, consistent with an M2-like anti-inflammatory phenotype that may enhance their ability to
431 interact with and internalize microorganisms (Fig. 2F and Supplementary Fig. 3E). In contrast, the
432 CD14$^+$CD16$^-$ subset displayed higher expression of CD86, a marker associated with an M1-like pro-
433 inflammatory state. Following Mtb infection, these phenotypic profiles were largely preserved:
434 CD16$^+$ cells continued to express higher levels of CD163, CD209, and MARCO, whereas CD16$^-$ cells
435 maintained a more pro-inflammatory profile. The main exception was CD169, a type-I interferon
436 (IFN-I)-inducible activation marker, which was upregulated in both subsets after infection, most
437 notably in CD16$^-$ cells, leading to comparable expression levels between CD14$^+$CD16$^-$ and
438 CD14$^+$CD16$^+$ subpopulations (Fig. 2F and Supplementary Fig. 3E). Consistent with an activated IFN-I
439 response, bulk mRNA analysis of Mtb-infected AMLs revealed increased expression of several IFN-
440 I–inducible genes upon Mtb infection, including *MX1*, *MX2*, interferon-stimulated gene 15 (*ISG15),*
441 and *SIGLEC1* (CD169) (Fig. 2G). Collectively, this difference in expression profiles highlights a

442 functional dichotomy between these AML subsets, which likely shapes their contributions to Mtb
443 infection.

444 To place these findings in a more physiological context, we performed a complementary
445 analysis using publicly available transcriptomic data from freshly isolated hAMs from healthy
446 donors, which were then infected *ex vivo* with Mtb (43). This dataset tracked transcriptional
447 dynamics over 72h. In line with our observations, infected hAMs upregulated activation genes (e.g
448 *CD274* (PD-L1), *CD38*, *TNF*, *IL6*) and progressively downregulated the anti-inflammatory regulator
449 *FCGR3A* (CD16) (Fig. 3A). Beyond this predefined macrophage gene signature, the broader
450 transcriptomic landscape of infected hAMs revealed strong induction of chemokines, ISGs and
451 inflammatory mediators (Fig. 3A-B). The IFN-I axis was characterized by the induction of several
452 ISGs, including *CXCL10* (Fig. 3B), a pro-inflammatory chemokine linked to tissue pathology (44),
453 further reinforcing the inflammatory potential of infected AMs. Additional ISGs comprised *IFIT1*,
454 which is required for IFN-β–mediated control of intracellular bacterial infection in macrophages
455 (45), as well as the IFITM family, *MX1,* and *MX2*, classically described as viral restriction factors but
456 also relevant to bacterial infection dynamics. Further antiviral mediators included *ISG15*, which not
457 only exerts antiviral effects but also regulates cellular metabolism and mitochondrial activity (46),
458 as well as *ISG20* and *OAS3*, the latter of which is expressed selectively in response to virulent Mtb
459 infection (47). Induction of *RSAD2* (viperin), a key effector of IFN-I signaling known as a restriction
460 factor of viral infection (48), recently shown to support persistent viral infection (49), points toward
461 an IFN-I–dominated response. Importantly, transcriptional regulators such as *IRF7*, a master
462 controller of IFN-I signaling implicated in M1-to-M2 macrophage transitions (50), and *NEURL3*,
463 which promotes innate antiviral defense by catalyzing K63-linked ubiquitination of IRF7 (51), suggest
464 a layered regulation of this IFN-I-driven program (Fig. 3A-B). Complementary reactome analysis
465 revealed significant enrichment of IFN-I signaling, interleukin signaling, IL-10 and IL-4/IL-13
466 pathways, and chemokine receptor signaling in hAMs after Mtb-infection (Fig. 3C).

467 Together, these data establish that Mtb-infected hAMs adopt a strong pro-inflammatory,
468 IFN-I–dominated transcriptional profile, characterized by chemokine-driven leukocyte recruitment,
469 antiviral-like defense programs, and selective downregulation of complement and autophagy
470 regulators. In line with our AML findings, these transcriptomic profiles underscore that Mtb
471 infection drives dynamic reprogramming of AMs, balancing antimicrobial and inflammatory
472 pressures with compensatory regulatory pathways that may ultimately contribute to bacterial
473 persistence.

474

475 **Benchmarking of Anti-TB Drugs in the Human Alveolar Macrophage-Like Cell Model.**

476 To assess whether AMLs represent a relevant human *in vitro* platform for testing novel anti-
477 TB compounds, we benchmarked their response to three drug categories: standard-of-care
478 antibiotics, host-directed therapies, and virulence-targeting therapies. We first measured bacterial
479 burden using luminescence readouts from AMLs infected with H37Rv::lux (Fig. 4A). Importantly,
480 none of the compounds tested displayed detectable cytotoxicity at the concentrations used
481 (Supplementary Fig. 4), ensuring that the observed effects reflected genuine modulation of bacterial
482 replication rather than host cell toxicity. As expected, most standard-of-care antibiotics markedly
483 reduced luminescence, except pyrazinamide (PZA). Both virulence factors–targeting compounds
484 achieved modest reductions in luminescence intensity (Fig. 4A). Among host-directed therapy
485 candidates, only doramapimod (DORA, (52)) demonstrated a strong inhibitory effect on
486 luminescence. To validate these findings, we quantified viable bacteria by CFU counts, the gold
487 standard method for assessing Mtb replication (Fig. 4B). All standard-of-care antibiotics, including
488 PZA, significantly suppressed bacterial replication. In addition, most host-directed therapies and
489 virulence factor-targeting compounds reduced CFU counts. By contrast, ibuprofen (IBU), a non-
490 steroidal anti-inflammatory drug (NSAID, (53)), and unexpectedly DORA failed to yield statistically
491 significant effects on CFU counts (Fig. 4B).

492 Beyond antibacterial activity, we evaluated the immunomodulatory potential of these
493 compounds in AMLs following Mtb infection (Fig. 4C). To this end, we measured the secretion of
494 proinflammatory cytokines TNF-α and IL-6, as they are recognized correlates of disease severity in
495 TB patients (54). All standard-of-care antibiotics significantly reduced TNF-α production, but only
496 linezolid (LZD), and rifampicin (RIF), also markedly decreased IL-6 levels (Fig. 4C). Among the
497 virulence factors targeting compounds, ethoxzolamide (ETZ), uniquely suppressed TNF-α without
498 affecting IL-6 (Fig. 4C). Within the host-directed therapy group, metformin (MET) — a biguanide
499 anti-diabetic agent repurposed for TB research through activation of AMP-activated protein kinase
500 (AMPK), thereby promoting autophagy and enhancing mitochondrial reactive oxygen species
501 (mROS) production (55) — and DORA both significantly reduced TNF-α and IL-6 levels (Fig. 4C).
502 Taken together, these findings reveal that the AML model can identify distinct immunomodulatory
503 profiles across various classes of anti-TB compounds, reinforcing its significance as a physiologically
504 relevant hAM platform and as a practical alternative to MDM- or THP-1-based approaches.
505

506 **Human Airway Air–Liquid Interface (ALI) System Recapitulates the Human Pulmonary**
507 **Environment and Supports Mtb Infection.**

508 Mtb is widely recognized as an intracellular pathogen that primarily resides within
509 macrophages. However, during active TB, a substantial proportion of the bacilli are present in the
510 extracellular environment of the airways. In this milieu, extracellular Mtb directly engages the
511 airway epithelium, triggering, in turn, pattern recognition receptor-mediated signaling cascades
512 that culminate in the secretion of pro-inflammatory cytokines and chemokines (22, 56). This
513 epithelial response not only amplifies local inflammation and modulates resident macrophages but
514 also recruits and activates additional leukocytes, ultimately influencing the course of infection and
515 incidence of tissue pathology.

516 To model the epithelial response to Mtb and its contribution to airway inflammation, we
517 employed an airway organoid/ALI culture system, an *in vitro* approach that mimics the structure
518 and function of bronchiolar epithelium (Fig. 5A) ((26–28, 57). To confirm the model's relevance, we
519 first examined whether it recapitulates key features of the airway epithelium. Epifluorescence and
520 light microscopy analysis of the ALI cultures revealed a densely packed epithelial layer with a healthy
521 tissue architecture. The presence of wave-like structures and surface texture variations may reflect
522 the formation of cilia or microvilli, hallmark features of differentiated airway epithelial cells (Fig.
523 5B). Indeed, analysis of H&E staining demonstrated a thin, regular, and well-organized cell layer,
524 with a morphology typical of healthy airway tissue (Fig. 5C). The presence of nuclei at varying heights
525 and structures suggestive of an apical ciliated border are consistent with a pseudostratified, ciliated
526 epithelium (Fig. 5C). Additionally, Alcian Blue staining demonstrated secretory cells distributed
527 throughout the epithelial layer, together with apical acidic mucins and apical mucus accumulation,
528 indicative of mucosecretory differentiation (Fig. 5D). To complement these findings, we performed
529 SEM to visualize the apical architecture of the ALI cultures directly. The surface ultrastructure
530 confirmed the presence of ciliated epithelial cells with numerous surface cilia, scattered microvilli,
531 and goblet cells, supporting the differentiated states of the ALI cultures (Fig. 5E). Assessment of
532 epithelial integrity and paracellular permeability demonstrated that ALI cultures form a functional
533 barrier, as indicated by low dextran flux and high transepithelial electrical resistance values (Fig. 5F-
534 G). Finally, live imaging using epifluorescence and light microscopy revealed continuous,
535 synchronized ciliary beating, a key physiological mechanism of mucociliary clearance, as shown in
536 Supplementary Movie 1. These observations indicate that the ALI cultures not only exhibit structural
537 features of airway epithelium but also preserve essential functional properties.

538 Next, we examined how ALI cultures respond to Mtb infection. To mimic the physiological
539 route of airborne exposure, Mtb was applied exclusively to the apical surface of differentiated ALI
540 cultures (22, 23), and mycobacterial replication was monitored over six days by measuring
541 bioluminescence and live bacterial load (CFU). Strikingly, rather than replicating, Mtb showed a
542 progressive decline over time in both luminescence and viable counts, indicating not only a lack of
543 replication but a potential loss of bacterial viability in this model (Fig. 5H), as previously described
544 in Mtb-infected airway organoids (26). No bacteria were detected in the basal compartment at any
545 time point, indicating that Mtb did not alter the epithelial barrier and remained confined to the
546 apical side (Fig. 5I). Epifluorescence and light microscopy, as well as SEM, confirmed this observation
547 and further revealed intimate interactions between Mtb and the cilia of ciliated epithelial cells at
548 the apical surface (Fig. 5J). Collectively, these findings demonstrate that while ALI cultures allow
549 Mtb to colonize the apical airway, they still function as a barrier against bacterial translocation and
550 deeper invasion, recapitulating a key aspect of the airway's innate defense.
551
552 **Benchmarking of Anti-TB Drugs in a Human Airway Air–Liquid Interface (ALI) System.**

553 To assess whether anti-TB compounds could inhibit extracellular Mtb replication or
554 modulate epithelial cell responses to infection, we benchmarked their responses across the three
555 drug categories. As such, Mtb-infected ALI cultures were exposed to anti-TB compounds, and
556 bacterial load at the apical surface was measured six days later by both bioluminescence and CFU
557 analyses. All standard-of-care drugs, except PZA, significantly reduced luminescence intensity,
558 indicating they effectively crossed the epithelial barrier to inhibit bacterial replication (Fig. 6A). In
559 contrast, no effect was observed following treatment with host-directed therapies or virulence
560 factors-targeting compounds. CFU analysis further supported these observations, revealing that
561 only INH, RIF, and Moxifloxacin (MXF), significantly suppressed bacterial growth (Fig. 6B). In parallel,
562 LZD reduced luminescence but failed to lower viable counts (Fig. 6A-B). Together, these results
563 demonstrate that the ALI model can effectively distinguish compounds with direct antibacterial
564 activity from those that primarily target host responses or bacterial virulence mechanisms.
565 Finally, we investigated whether these compounds modulate the inflammatory response in
566 ALI cultures, focusing on IL-6 and IL-8 secretion, which are linked to lung inflammation and TB
567 pathology. As expected, Mtb infection led to a significant increase in IL-6 and IL-8 production by
568 epithelial cells (Fig. 6C). Notably, despite their vigorous bactericidal activity, standard-of-care drugs
569 did not reduce IL-6 secretion, whereas MXF and PZA modestly decreased IL-8 levels. Among all
570 tested compounds, ETZ was unique in enhancing inflammation, reflected in a significant level of IL-

571 6 production without influencing that of IL-8 (Fig. 6C). Although none of the host-directed therapies
572 compounds significantly reduced the bacterial load, most of them modulated the cytokine profile in
573 this system: IBU, and DORA significantly reduced IL-6 secretion, while aspirin (ASA), IBU, and MET
574 decreased IL-8 release (Fig. 6C). Collectively, these results demonstrate that the ALI model can
575 capture drug-induced modulation of epithelial inflammatory responses independently of
576 antibacterial efficacy.

577 **4.** DISCUSSION

578 In our study, we developed and tested a dual *in vitro* platform that includes human AML and
579 airway ALI cultures. This setup is designed to evaluate various anti-TB compounds, including
580 standard antibiotics, host-directed therapies, and strategies targeting virulent pathogenic factors.
581 By mimicking different niches of the human lung that Mtb encounters during infection, particularly
582 the airway spaces where this pathogen interacts with resident macrophages and epithelial cells, we
583 can comprehensively study the effects of these compounds in an unprecedented manner.

584 The AML model closely mirrors the biology of primary hAMs. Adapted from previous report
585 (17, 18), this study recapitulates the key characteristics of primary hAMs, including strong
586 expression of the transcription factor PPAR-γ and high levels of signature markers such as CD206,
587 CD64, CD14, CD16, CD163, CD169, CXCR4, and PD-L1. These cellular findings are reinforced by an
588 integrative transcriptomic comparison of AMLs and MDMs from the same differentiation framework
589 (17, 18). AMLs primarily express tissue-resident and immunoregulatory modules, such as *MRC1*
590 (CD206), *MARCO*, *FCGR3A* (CD16), and *CD274* (PD-L1), whereas MDMs tend to express pro-
591 inflammatory and matrix-remodeling genes, including *TNF*, *FCAR*, *CD86,* and *MMP9*. Unbiased
592 differential expression reveals that AML-upregulated genes, including *ABHD5* (which suppresses NF-
593 κB–dependent MMPs), *AOC3* (involved in airway immune regulation), and *KLF4* (involved in STAT6-
594 coupled activation), form a lung-adapted lipid-centric program (58, 59). In contrast, lower levels of
595 *GALM* and *TRAF1* suggest distinct glucose metabolism and reduced NF-κB/inflammasome activity
596 compared to MDMs. Gene-ontology enrichment suggests that macrophages are shaped by
597 surfactant and ongoing epithelial interactions in the alveolar niche, aligning with expectations of
598 GPCR signaling, inflammatory response regulation, and lipid homeostasis. These characteristics align
599 with transcriptomic and phenotypic analyses of hAM *in vivo*, in which PPAR-γ functions as the
600 master regulator of lipid metabolism and anti-inflammatory programming (6).

601 Importantly, AML recapitulated the functional heterogeneity of AMs observed across
602 species during Mtb infection. In the mouse model, CD38 stratified AMs into distinct subsets: $CD38^{high}$
603 cells exhibited enhanced microbicidal programs and reduced permissiveness, whereas $CD38^{low}$ AMs
604 were comparatively permissive (60). In human MDMs differentiated with conditioned medium from
605 Mtb-infected macrophages, we previously identified a $CD16^{+}CD163^{+}MerTK^{+}$ subset with an anti-
606 inflammatory profile that was more permissive to Mtb infection (24). Strikingly, this population was
607 also detected in the lungs of non-human primates, reinforcing its physiological relevance (24).
608 Consistent with these findings, the AML model revealed a similar functional dichotomy defined by
609 the partitioning of CD14 and CD16. Although CD38 did not distinguish resistant and permissive

610 subsets as observed in mice, both CD16 subsets upregulated CD38 equally upon infection. The
611 $CD14^{+}CD16^{+}$ subset displayed an M2-like cell-surface marker signature (e.g., CD163, MARCO, and
612 CD209), along with higher baseline CD169 expression, which correlated with a higher burden of
613 intracellular bacteria. In contrast, the $CD14^{+}CD16^{-}$ subset showed an M1-like profile (e.g., CD86) and
614 reduced susceptibility to infection. Indeed, resident AMs exhibit a more permissive phenotype
615 compared to monocyte-derived AMs, partly due to metabolic constraints that limit pro-
616 inflammatory activation (7, 60). Moreover, by high-dimensional flow cytometry analysis, we
617 revealed distinct activation states in macrophages driven by infection, underscoring the AML
618 model's ability to recapitulate the complex phenotypic diversity observed in macrophages across
619 lung niches during Mtb infection *in vivo* (7, 61). To further contextualize our results within a
620 physiological framework, we integrated data from freshly isolated hAMs infected *ex vivo* with Mtb
621 (43). Infected hAMs upregulated activation markers (e.g, *CD274* (PD-L1), *TNF*, *IL6*) while
622 progressively losing anti-inflammatory regulator *FCGR3A* (CD16). This shift was accompanied by the
623 induction of inflammatory chemokines, such as *CCL20*, *CCL4*, and *CXCL10*, which coordinate immune
624 cell recruitment but can also drive tissue pathology. In addition, a strong induction of ISGs (e.g.,
625 *IFIT1*, *ISG15*, *MX1*, *OAS3*, *RSAD2*) underscored a dominant IFN-I axis, while regulators such as *IRF7*
626 and *NEURL3* suggested layered control of this program. Thus, our data establish AMLs as a model
627 that not only mirrors the functional dichotomy found in AMs in the lung but also reveals the layered
628 activation states that govern host–pathogen interactions during Mtb infection. This complexity
629 provides a physiologically relevant platform, particularly valuable for identifying new compounds
630 that modulate host–pathogen interactions in TB.

631 To explore this potential, we benchmarked various anti-TB drugs using the AML model. We
632 observed significant differences in their antibacterial and immunomodulatory properties. While
633 most standard-of-care antibiotics effectively reduced intracellular bacterial load in AMLs, PZA's
634 activity was initially underestimated by luminescence and later confirmed by CFU, highlighting the
635 need for multiple, complementary assays. Interestingly, however, Heifets and colleagues reported
636 that PZA exerts neither bacteriostatic nor bactericidal effects against Mtb in MDMs, independent of
637 the macrophage activation status (62). This finding aligns with other pioneering studies that have
638 established PZA as primarily effective *in vivo* but poorly potent *in vitro* (63–66). Yet, the significant
639 effect of PZA we now report in AMLs is probably reflective of their hAM biology, which is known for
640 its weaker microbicidal activity in early Mtb containment (6, 7, 60, 61, 67). While direct comparisons
641 of PZA efficacy in AML versus MDM models (derived from the same donor) remain to be explored,

642 the hAM-like phenotype of AMLs suggests they better recapitulate lung-specific drug responses
643 targeting the alveolar compartment.

644 In addition, host-directed therapies and treatments targeting virulence factors in infected
645 AMLs showed variable antibacterial effects, often modulating inflammatory signals, such as TNF-α
646 and IL-6. Studies using MDMs or THP-1 cells similarly report host-directed therapies targeting
647 inflammatory pathways (e.g., autophagy inducers, metabolic shifting agents), but often require
648 exaggerated doses to modulate the cytokine response (68). Moreover, the reported impact of
649 virulence-targeting factors on immune signaling appears to be highly target-specific, with some
650 factors attenuating IFN-I production (via cGAS) by blocking the secretion of EsxA/EsxB. In contrast,
651 others modulate virulence-associated transcriptional programs without apparent suppression of
652 cytokine release (69). Yet, systematic evaluations of immune modulation mediated by virulence-
653 targeting factors in human lung-resident macrophages remain scarce. Taken together, the observed
654 uncoupling between bacterial control and cytokine modulation in AMLs indicates that this cell
655 model is sensitive to host-directed therapies and interventions targeting virulence factors, and
656 underscores its value as a physiologically relevant platform for targeting host-pathogen interactions
657 aligned with hAM biology. Notably, recent findings validating iPSC-derived macrophages as a
658 platform for Mtb infection and drug testing (70) have highlighted their scalability and physiological
659 relevance for high-throughput screening (HTS). Our data further emphasize that AMLs exhibit a
660 phenotype more closely resembling *in vivo* alveolar macrophages and offer additional practical
661 advantages, including faster and easier generation and the ability to capture interindividual
662 variability in treatment responses, while also holding potential for HTS applications.

663 Another key aspect of this study is our focus on the airway epithelium, which is increasingly
664 recognized as vital in modulating immune responses during active TB. In line with recent reports
665 (22, 56), we found that although Mtb can colonize the apical surface of airway epithelial cells, it fails
666 to traverse the epithelial barrier or replicate robustly, highlighting the airway epithelium's intrinsic
667 defensive capacity. This observation aligns with clinical and experimental evidence suggesting that
668 airway epithelial cells act as gatekeepers through mucociliary clearance and innate defense
669 pathways, thereby limiting bacterial dissemination into deeper tissues (56, 71, 72). Interestingly,
670 bacterial loads in the ALI system naturally decline over 6 days of infection, likely due to epithelial
671 innate immune mechanisms, including the production of antimicrobial peptides such as β-Defensin-
672 1 and RNAse7, as we previously reported in Mtb–infected airway organoids (26). Our results
673 demonstrate a clear discriminating capacity between treatments: first-line drugs such as INH, RIF,
674 and MXF significantly suppressed bacterial growth, whereas LZD, a bacteriostatic antibiotic,

675 efficiently impairs protein synthesis, as shown with a substantial reduction of luminescence but
676 failed to impact CFUs, reflecting discrepancies between metabolic readouts and bacterial viability
677 assays also noted in macrophage-based assays. This apparent lack of effect likely reflects the
678 intrinsic limitation of bacterial growth in the ALI system, where bacterial loads naturally decline over
679 time, thereby masking any additional contributions from bacteriostatic drug activity. PZA was
680 ineffective, consistent with previous studies reporting its limited or delayed activity *in vitro* due to
681 pH-dependent activation. This underscores the translational potential of the ALI system in
682 predicting which drugs can access and remain active at the airway interface.

683 The ALI model also facilitated the assessment of epithelial-driven inflammatory responses
684 and their modulation through therapeutic interventions. As expected, Mtb infection led to
685 significant secretion of pro-inflammatory cytokines IL-6 and IL-8, aligning with their established roles
686 in driving inflammation and leukocyte recruitment in TB pathology. Although standard-of-care
687 antibiotics exhibited the predicted bactericidal properties, they did not significantly reduce cytokine
688 secretion, indicating that merely clearing the pathogen is insufficient to mitigate epithelial-driven
689 inflammation. This pattern is consistent with features of the airway ALI context, where Mtb largely
690 remains at the apical surface and epithelial signaling is dominated by apical and endosomal PRRs
691 (e.g., TLRs and C-type lectins) (22, 56). In contrast, macrophages additionally integrate cytosolic cues
692 delivered by virulent Mtb via ESX-1 secretion system, which exports virulence factors such as ESAT-
693 6 that permeabilize the phagosomal membrane, allowing Mtb antigens to access the host cytosol
694 and activate cytosolic sensors (e.g., cGAS/STING, AIM2, NLRs, RIG) (72–76). Accordingly, most
695 antibiotic therapies kill Mtb but leave behind PAMP-rich debris (lipoproteins, cell wall lipids, nucleic
696 acids) that continues to engage surface and endosomal PRRs (77, 78). By contrast, robust activation
697 of cytosolic sensors typically requires live, ESX-1-competent bacilli, an event unlikely to occur once
698 bacteria are non-viable under antibiotic treatment (73, 79). Together, these observations suggest
699 the need for adjunct host-directed strategies that modulate epithelial sensing pathways in addition
700 to pathogen killing.

701 Conversely, ETZ uniquely increased IL-6 secretion in the ALI system, suggesting possible off-
702 target pro-inflammatory effects. By comparison, host-directed therapies such as IBU, ASA, MET, and
703 DORA effectively attenuated IL-6 and/or IL-8 levels without altering bacterial load, demonstrating
704 the ALI model's ability to capture immunomodulatory effects independent of antimicrobial activity.
705 Collectively, these findings reinforce the relevance of the ALI model as a platform for exploring the
706 antimicrobial efficacy and immunomodulatory potential of anti-TB compounds in the airway
707 context. By emphasizing the extracellular niche of Mtb during active TB, rather than the purely

708 intracellular dynamics captured by macrophage-based models, the ALI system highlights the airway
709 epithelium's dual role as a barrier and as an active regulator of inflammation. Importantly, excessive
710 inflammation is a hallmark of severe TB and is strongly associated with tissue destruction and
711 disease progression (80). Thus, therapeutic strategies that combine pathogen clearance with
712 modulation of host inflammatory pathways may be particularly valuable, especially in advanced or
713 disseminated TB, where hyperinflammation exacerbates pathology and worsens clinical outcomes.
714 Our complementary macrophage and ALI models provide a unique framework to dissect these
715 processes. While AMLs capture intracellular niches where antibiotics and host-directed agents can
716 reduce both bacterial burden and proinflammatory signaling, ALIs reflect epithelial-driven
717 responses that remain largely unaffected by bacterial killing alone. Together, these models
718 demonstrate that compounds can differentially affect intracellular versus extracellular bacteria and
719 modulate immune responses in cell types that sense and respond to Mtb in fundamentally distinct
720 ways. This underscores the potential of combining antimicrobial activity with host-directed
721 modulation to more effectively treat severe TB.

722 In summary, our study validates and highlights the relevance of using a dual *in vitro* system
723 that integrates AML and airway ALI responses as a biologically relevant framework for dissecting the
724 intracellular and extracellular niches of Mtb within the lung. By recapitulating key features of
725 primary human airway mucosa (hAMs) and the epithelial barrier, this approach enables a side-by-
726 side assessment of the antimicrobial potency and immunomodulatory capacity of anti-TB
727 compounds. The AML model revealed that macrophage activation states, particularly those
728 associated with CD16 expression, critically influence bacterial burden and immune activation. In
729 contrast, the ALI system highlighted the impact on epithelial-driven inflammation. Collectively,
730 these findings position AML and ALI cultures as complementary, tractable models that may bridge
731 the gap between reductionist *in vitro* assays and the complex *in vivo* lung environment, offering a
732 valuable system for advancing both drug discovery and host-directed therapeutic strategies in TB.

5. AUTHOR CONTRIBUTIONS

Conceptualization: CCBB, NF, FD, CV, GL-V, and CC. *Methodology:* CCBB, NF, TB, JMS-L, EN, PV, AM, RP, CV, GL-V, and CC. *Investigation*: CCBB, NF, TB, MP, BS, DP, JMS-L, BMA-C, EN, PV, AM, and CC. *Resources:* EN, NG, JM, RP, BR-M, FD, ON, EM, CV, GL-V, RV and CC. *Formal Analysis:* CCBB, NF, TB, MP, JMS-L, BMA-C, EN, PV, GL-V, and CC. Writing: CCBB, NF, GLV, and CC. *Visualization:* CCBB, NF, TB, MP, JMS-L, BMA-C, EN, PV, AM, RP, CV, and CC. *Supervision:* FD, CV, EM, GL-V, and CC. *Project Administration:* CC. *Funding acquisition:* RP, ON, EM, CV, GL-V, and CC. Corresponding authors: CCBB and CC are responsible for the ownership and responsibility that are inherent to aspects of this study.

6. DECLARATION OF INTERESTS

The authors declare no competing interests.

745 **7.** ACKNOWLEDGMENTS

746 We would like to acknowledge Myriam Ben-Neji and Genotoul Anexplo-IPBS for access to
747 the BSL-3 facilities; the Genotoul TRI-IPBS facilities for imaging; and histology platform at IPBS. We
748 thank Vanessa Soldan and Stephanie Balor (CBI) for TEM, Isabelle Fourquaux (CMEAB) for SEM work,
749 and Yoann Rombouts and Claude Gutierrez for obtaining the integrative plasmid pMV30-hsp-Lux13
750 (Addgene #26161) and constructing the strain H37Rv::lux, respectively. We thank Jean-Philippe
751 Girard for giving access to the Zeiss Axio imager M2 microscope (IPBS). We thank Drs. Aurelien
752 Brindel, Gavin Plat, and Valentin Heluain from Toulouse hospital for BAL patient samples.
753 Additionally, we thank all members of ITHEMYC Consortium (https://tbvi.eu/our-projects/ithemyc/)
754 for their scientific input, and in particular the Global Health Medicines R&D and Sample
755 Management departments at GLAXOSMITHKLINE INVESTIGACION Y DESARROLLO SL (GSK) for
756 providing the benchmarking compounds. The ITHEMYC project, "Novel immunotherapies for
757 tuberculosis and other mycobacterial diseases", is funded by the European Union's Health and
758 Digital Executive Agency (HaDEA) under Grant Agreement number 101080462 and by UK Research
759 and Innovation (UKRI). This work was also supported by the Centre National de la Recherche
760 Scientifique, the Université Paul Sabatier, the Institut National de la Santé et de la Recherche
761 Médicale, the Agence Nationale de la Recherche, the Agence Nationale de Recherche sur le Sida et
762 les hépatites virales (ANRS MIE), Sidaction, and the Fondation pour la Recherche Médicale.
763 Postdoctoral fellows C.B., T.B., and J.M.S-L. are recipients of the ITHEMYC project (Grant Agreement
764 number 101080462), Bill and Melinda Gates Foundation INV-046428, and SECTEI/071/2024
765 (Mexican postdoctoral scholarship in academic or research institutions abroad with international
766 recognition) scholarships, respectively. A doctoral fellowship from ANRS MIE supported N.F.

767 **8.** REFERENCES

768 1. WHO. 2024. Global Tuberculosis Report 2024. https://www.who.int/teams/global-programme-on-
769 tuberculosis-and-lung-health/tb-reports/global-tuberculosis-report-2024. Retrieved 28 July 2025.

770 2. Shao Y, Song H, Li G, Li Y, Li Y, Zhu L, Lu W, Chen C. 2021. Relapse or Re-Infection, the Situation of
771 Recurrent Tuberculosis in Eastern China. Front Cell Infect Microbiol 11:638990.

772 3. CDC. 2025. Clinical Overview of Latent Tuberculosis Infection. Tuberc TB.
773 https://www.cdc.gov/tb/hcp/clinical-overview/latent-tuberculosis-infection.html. Retrieved 22 July
774 2025.

775 4. Koeken V a. CM, Verrall AJ, Netea MG, Hill PC, van Crevel R. 2019. Trained innate immunity and
776 resistance to Mycobacterium tuberculosis infection. Clin Microbiol Infect Off Publ Eur Soc Clin
777 Microbiol Infect Dis 25:1468–1472.

778 5. Aegerter H, Lambrecht BN, Jakubzick CV. 2022. Biology of lung macrophages in health and disease.
779 Immunity 55:1564–1580.

780 6. Huang L, Nazarova EV, Tan S, Liu Y, Russell DG. 2018. Growth of Mycobacterium tuberculosis in vivo
781 segregates with host macrophage metabolism and ontogeny. J Exp Med 215:1135–1152.

782 7. Russell DG, Simwela NV, Mattila JT, Flynn J, Mwandumba HC, Pisu D. 2025. How macrophage
783 heterogeneity affects tuberculosis disease and therapy. Nat Rev Immunol 25:370–384.

784 8. Cohen SB, Gern BH, Delahaye JL, Adams KN, Plumlee CR, Winkler JK, Sherman DR, Gerner MY, Urdahl
785 KB. 2018. Alveolar Macrophages Provide an Early Mycobacterium tuberculosis Niche and Initiate
786 Dissemination. Cell Host Microbe 24:439-446.e4.

787 9. Ginhoux F, Schultze JL, Murray PJ, Ochando J, Biswas SK. 2016. New insights into the multidimensional
788 concept of macrophage ontogeny, activation and function. Nat Immunol 17:34–40.

789 10. Neupane AS, Willson M, Chojnacki AK, Vargas E Silva Castanheira F, Morehouse C, Carestia A, Keller
790 AE, Peiseler M, DiGiandomenico A, Kelly MM, Amrein M, Jenne C, Thanabalasuriar A, Kubes P. 2020.
791 Patrolling Alveolar Macrophages Conceal Bacteria from the Immune System to Maintain Homeostasis.
792 Cell 183:110-125.e11.

793 11. Mould KJ, Moore CM, McManus SA, McCubbrey AL, McClendon JD, Griesmer CL, Henson PM, Janssen
794 WJ. 2021. Airspace Macrophages and Monocytes Exist in Transcriptionally Distinct Subsets in Healthy
795 Adults. Am J Respir Crit Care Med 203:946–956.

796 12. Bussi C, Gutierrez MG. 2019. Mycobacterium tuberculosis infection of host cells in space and time.
797 FEMS Microbiol Rev 43:341–361.

798 13. Lerner TR, Borel S, Gutierrez MG. 2015. The innate immune response in human tuberculosis. Cell
799 Microbiol 17:1277–1285.

800 14. Shah PT, Tufail M, Wu C, Xing L. 2022. THP-1 cell line model for tuberculosis: A platform for in vitro
801 macrophage manipulation. Tuberc Edinb Scotl 136:102243.

802 15. Choi S, Choi J, Cheon S, Song J, Kim S-Y, Kim J-E, Nam D-H, Manzar G, Kim S-M, Kang H-S, Kim KK,
803 Jeong SH, Lee J-H, Park E-K, Lee M, Lee H-A, Kim K-S, Park H-J, Oh WK, Park C, Lee CH, Kim E-M. 2022.
804 Pulmonary fibrosis model using micro-CT analyzable human PSC-derived alveolar organoids
805 containing alveolar macrophage-like cells. Cell Biol Toxicol 38:557–575.

806 16. Kang JS, Lee Y, Lee Y, Gil D, Kim MJ, Wood C, Delorme V, Lee JM, Ko K-C, Kim J-H, Lee M-O. 2025.
807 Generation of induced alveolar assembloids with functional alveolar-like macrophages. Nat Commun
808 16:3346.

809 17. Pahari S, Neehus A-L, Trapnell BC, Bustamante J, Casanova J-L, Schlesinger LS. 2024. Protocol to
810 develop human alveolar macrophage-like cells from mononuclear cells or purified monocytes for use
811 in respiratory biology research. STAR Protoc 5:103061.

812 18. Pahari S, Arnett E, Simper J, Azad A, Guerrero-Arguero I, Ye C, Zhang H, Cai H, Wang Y, Lai Z, Jarvis N,
813 Lumbreras M, Maselli DJ, Peters J, Torrelles JB, Martinez-Sobrido L, Schlesinger LS. 2023. A new
814 tractable method for generating human alveolar macrophage-like cells in vitro to study lung
815 inflammatory processes and diseases. mBio 0:e00834-23.

816 19. Fulcher ML, Gabriel S, Burns KA, Yankaskas JR, Randell SH. 2005. Well-differentiated human airway
817 epithelial cell cultures. Methods Mol Med 107:183–206.

818 20. Gard AL, Luu RJ, Miller CR, Maloney R, Cain BP, Marr EE, Burns DM, Gaibler R, Mulhern TJ, Wong CA,
819 Alladina J, Coppeta JR, Liu P, Wang JP, Azizgolshani H, Fezzie RF, Balestrini JL, Isenberg BC, Medoff BD,
820 Finberg RW, Borenstein JT. 2021. High-throughput human primary cell-based airway model for
821 evaluating influenza, coronavirus, or other respiratory viruses in vitro. Sci Rep 11:14961.

822 21. Jirikowski GF, Caldwell JD, Stumpf WE, Pedersen CA. 1990. Topography of oxytocinergic estradiol
823 target neurons in the mouse hypothalamus. Folia Histochem Cytobiol 28:3–9.

824 22. Barclay AM, Ninaber DK, van Veen S, Hiemstra PS, Ottenhoff THM, van der Does AM, Joosten SA.
825 2023. Airway epithelial cells mount an early response to mycobacterial infection. Front Cell Infect
826 Microbiol 13.

827 23. Joy N, Deshpande A, Lingamallu SM, Prabantu VM, Naveenkumar CN, Bharathkumar K, Bhat S,
828 Alvarado-Martinez Z, Livraghi-Butrico A, Hagood JS, Boucher RC, Lafkas D, Byrd KM, Narayanan S,
829 Shandil RK, Guha A. 2024. Notch signaling stabilizes lengths of motile cilia in multiciliated cells in the
830 lung. BioRxiv Prepr Serv Biol 2024.12.12.628112.

831 24. Lastrucci C, Bénard A, Balboa L, Pingris K, Souriant S, Poincloux R, Al Saati T, Rasolofo V, González-
832 Montaner P, Inwentarz S, Moraña EJ, Kondova I, Verreck FAW, Sasiain M del C, Neyrolles O,
833 Maridonneau-Parini I, Lugo-Villarino G, Cougoule C. 2015. Tuberculosis is associated with expansion
834 of a motile, permissive and immunomodulatory CD16(+) monocyte population via the IL-10/STAT3
835 axis. Cell Res 25:1333–1351.

836 25. Mascarau R, Woottum M, Fromont L, Gence R, Cantaloube-Ferrieu V, Vahlas Z, Lévêque K, Bertrand F,
837 Beunon T, Métais A, El Costa H, Jabrane-Ferrat N, Gallois Y, Guibert N, Davignon J-L, Favre G,
838 Maridonneau-Parini I, Poincloux R, Lagane B, Bénichou S, Raynaud-Messina B, Vérollet C. 2023.
839 Productive HIV-1 infection of tissue macrophages by fusion with infected CD4+ T cells. J Cell Biol
840 222:e202205103.

841 26. Iakobachvili N, Leon-Icaza SA, Knoops K, Sachs N, Mazères S, Simeone R, Peixoto A, Bernard C, Murris-
842 Espin M, Mazières J, Cam K, Chalut C, Guilhot C, López-Iglesias C, Ravelli RBG, Neyrolles O, Meunier E,
843 Lugo-Villarino G, Clevers H, Cougoule C, Peters PJ. 2022. Mycobacteria–host interactions in human
844 bronchiolar airway organoids. Mol Microbiol 117:682–692.

845 27. Sachs N, Papaspyropoulos A, Zomer-van Ommen DD, Heo I, Böttinger L, Klay D, Weeber F, Huelsz-
846 Prince G, Iakobachvili N, Amatngalim GD, de Ligt J, van Hoeck A, Proost N, Viveen MC, Lyubimova A,
847 Teeven L, Derakhshan S, Korving J, Begthel H, Dekkers JF, Kumawat K, Ramos E, van Oosterhout MF,
848 Offerhaus GJ, Wiener DJ, Olimpio EP, Dijkstra KK, Smit EF, van der Linden M, Jaksani S, van de Ven M,
849 Jonkers J, Rios AC, Voest EE, van Moorsel CH, van der Ent CK, Cuppen E, van Oudenaarden A,
850 Coenjaerts FE, Meyaard L, Bont LJ, Peters PJ, Tans SJ, van Zon JS, Boj SF, Vries RG, Beekman JM,
851 Clevers H. 2019. Long-term expanding human airway organoids for disease modeling. EMBO J
852 38:e100300.

853 28. Péricat D, Leon-Icaza SA, Sanchez Rico M, Mühle C, Zoicas I, Schumacher F, Planès R, Mazars R, Gros
854 G, Carpinteiro A, Becker KA, Izopet J, Strub-Wourgaft N, Sjö P, Neyrolles O, Kleuser B, Limosin F,
855 Gulbins E, Kornhuber J, Meunier E, Hoertel N, Cougoule C. 2022. Antiviral and Anti-Inflammatory
856 Activities of Fluoxetine in a SARS-CoV-2 Infection Mouse Model. Int J Mol Sci 23:13623.

857 29. Sanchez-Lopez JM, Juarez-Mancera MA, Bustamante B, Ruiz-Silvestre A, Espinosa M, Mendoza-
858 Almanza G, Ceballos-Cancino G, Melendez-Zajgla J, Maldonado V, Lizarraga F. 2024. Decoding
859 LINC00052 role in breast cancer by bioinformatic and experimental analyses. RNA Biol 21:1–11.

860 30. Calzada F, García-Hernández N, Bautista E, Sánchez-López JM, Valdes M, Velázquez C, Barbosa E.
861 2024. Understanding the Molecular Mechanisms of Incomptine A in Treating Non-Hodgkin Lymphoma
862 Associated with U-937 Cells: Bioinformatics Approaches, Part I. Pharm Basel Switz 18:5.

863 31. Schneider C, Nobs SP, Kurrer M, Rehrauer H, Thiele C, Kopf M. 2014. Induction of the nuclear receptor
864 PPAR-γ by the cytokine GM-CSF is critical for the differentiation of fetal monocytes into alveolar
865 macrophages. Nat Immunol 15:1026–1037.

866 32. Bharat A, Bhorade SM, Morales-Nebreda L, McQuattie-Pimentel AC, Soberanes S, Ridge K, DeCamp
867 MM, Mestan KK, Perlman H, Budinger GRS, Misharin AV. 2016. Flow Cytometry Reveals Similarities
868 Between Lung Macrophages in Humans and Mice. Am J Respir Cell Mol Biol 54:147–149.

869 33. Yu Y-RA, Hotten DF, Malakhau Y, Volker E, Ghio AJ, Noble PW, Kraft M, Hollingsworth JW, Gunn MD,
870 Tighe RM. 2016. Flow Cytometric Analysis of Myeloid Cells in Human Blood, Bronchoalveolar Lavage,
871 and Lung Tissues. Am J Respir Cell Mol Biol 54:13–24.

872 34. Desch AN, Gibbings SL, Goyal R, Kolde R, Bednarek J, Bruno T, Slansky JE, Jacobelli J, Mason R, Ito Y,
873 Messier E, Randolph GJ, Prabagar M, Atif SM, Segura E, Xavier RJ, Bratton DL, Janssen WJ, Henson PM,
874 Jakubzick CV. 2016. Flow Cytometric Analysis of Mononuclear Phagocytes in Nondiseased Human
875 Lung and Lung-Draining Lymph Nodes. Am J Respir Crit Care Med 193:614–626.

876 35. Shang S, Ji X, Zhang L, Chen J, Li C, Shi R, Xiang W, Kang X, Zhang D, Yang F, Dai R, Chen P, Chen S,
877 Chen Y, Li Y, Miao H. 2019. Macrophage ABHD5 Suppresses NFκB-Dependent Matrix
878 Metalloproteinase Expression and Cancer Metastasis. Cancer Res 79:5513–5526.

879 36. Dunkel J, Aguilar-Pimentel JA, Ollert M, Fuchs H, Gailus-Durner V, de Angelis MH, Jalkanen S, Salmi M,
880 Veres TZ. 2014. Endothelial amine oxidase AOC3 transiently contributes to adaptive immune
881 responses in the airways. Eur J Immunol 44:3232–3239.

882 37. Wu Y, Meng L, Zhan S, Li M, Huang J, Chen X, Chen L, Gao X, Chen H, Chen H, Zhong Y, Xu L, Xu Y.
883 2025. ITIH5-mediated fibroblast/macrophage crosstalk exacerbates cardiac remodelling after
884 myocardial infarction. J Transl Med 23:224.

885 38. Park S, Choi S-G, Yoo S-M, Son JH, Jung Y-K. 2014. Choline dehydrogenase interacts with SQSTM1/p62
886 to recruit LC3 and stimulate mitophagy. Autophagy 10:1906–1920.

887 39. Szafran BN, Borazjani A, Scheaffer HL, Crow JA, McBride AM, Adekanye O, Wonnacott CB, Lehner R,
888 Kaplan BLF, Ross MK. 2022. Carboxylesterase 1d Inactivation Augments Lung Inflammation in Mice.
889 ACS Pharmacol Transl Sci 5:919–931.

890 40. Moraes-Vieira PM, Yore MM, Sontheimer-Phelps A, Castoldi A, Norseen J, Aryal P, Simonyté Sjödin K,
891 Kahn BB. 2020. Retinol binding protein 4 primes the NLRP3 inflammasome by signaling through Toll-
892 like receptors 2 and 4. Proc Natl Acad Sci 117:31309–31318.

893 41. Liao X, Sharma N, Kapadia F, Zhou G, Lu Y, Hong H, Paruchuri K, Mahabeleshwar GH, Dalmas E,
894 Venteclef N, Flask CA, Kim J, Doreian BW, Lu KQ, Kaestner KH, Hamik A, Clément K, Jain MK. 2011.
895 Krüppel-like factor 4 regulates macrophage polarization. J Clin Invest 121:2736–2749.

896 42. Mirzaesmaeili A, Abdul-Sater AA. 2024. TRAF1 Deficiency in Macrophages Drives Exacerbated Joint
897 Inflammation in Rheumatoid Arthritis. Biomolecules 14:864.

898 43. Sadee W, Cheeseman IH, Papp A, Pietrzak M, Seweryn M, Zhou X, Lin S, Williams AM, Wewers MD,
899 Curry HM, Zhang H, Cai H, Kunsevi-Kilola C, Tshivhula H, Walzl G, Restrepo BI, Kleynhans L, Ronacher
900 K, Wang Y, Arnett E, Azad AK, Schlesinger LS. 2025. Human alveolar macrophage response to
901 Mycobacterium tuberculosis: immune characteristics underlying large inter-individual variability.
902 Commun Biol 8:950.

903 44. Tomita K, Freeman BL, Bronk SF, LeBrasseur NK, White TA, Hirsova P, Ibrahim SH. 2016. CXCL10-
904 Mediates Macrophage, but not Other Innate Immune Cells-Associated Inflammation in Murine
905 Nonalcoholic Steatohepatitis. Sci Rep 6:28786.

906 45. John SP, Sun J, Carlson RJ, Cao B, Bradfield CJ, Song J, Smelkinson M, Fraser IDC. 2018. IFIT1 Exerts
907 Opposing Regulatory Effects on the Inflammatory and Interferon Gene Programs in LPS-Activated
908 Human Macrophages. Cell Rep 25:95-106.e6.

909 46. Baldanta S, Fernández-Escobar M, Acín-Perez R, Albert M, Camafeita E, Jorge I, Vázquez J, Enríquez JA,
910 Guerra S. 2017. ISG15 governs mitochondrial function in macrophages following vaccinia virus
911 infection. PLoS Pathog 13:e1006651.

912 47. Leisching G, Cole V, Ali AT, Baker B. 2019. OAS1, OAS2 and OAS3 restrict intracellular M. tb replication
913 and enhance cytokine secretion. Int J Infect Dis IJID Off Publ Int Soc Infect Dis 80S:S77–S84.

914 48. Neil SJD, Sandrin V, Sundquist WI, Bieniasz PD. 2007. An interferon-alpha-induced tethering
915 mechanism inhibits HIV-1 and Ebola virus particle release but is counteracted by the HIV-1 Vpu
916 protein. Cell Host Microbe 2:193–203.

917 49. Zankharia U, Yi Y, Lu F, Vladimirova O, Karisetty BC, Wikramasinghe J, Kossenkov A, Collman RG,
918 Lieberman PM. 2024. HIV-induced RSAD2/Viperin supports sustained infection of monocyte-derived
919 macrophages. J Virol 98:e0086324.

920 50. Long Q, Rabi K, Cai Y, Li L, Huang S, Qian B, Zhong Y, Qi Z, Zhang Y, Huang K, Wang X, Chang L, Xie W,
921 Jiang H, Zhang H, Zhang J, Ren T, Wang Z, Teesalu T, Wu C, Lu L, Zhu Z, Chu Y, Santos HA, Liu Z, Zhao Q,
922 Ye X. 2025. Identification of splenic IRF7 as a nanotherapy target for tele-conditioning myocardial
923 reperfusion injury. Nat Commun 16:1909.

924 51. Qi F, Zhang X, Wang L, Ren C, Zhao X, Luo J, Lu D. 2022. E3 ubiquitin ligase NEURL3 promotes innate
925 antiviral response through catalyzing K63-linked ubiquitination of IRF7. FASEB J Off Publ Fed Am Soc
926 Exp Biol 36:e22409.

927 52. Gräb J, Suárez I, van Gumpel E, Winter S, Schreiber F, Esser A, Hölscher C, Fritsch M, Herb M,
928 Schramm M, Wachsmuth L, Pallasch C, Pasparakis M, Kashkar H, Rybniker J. 2019. Corticosteroids

929 inhibit Mycobacterium tuberculosis-induced necrotic host cell death by abrogating mitochondrial
930 membrane permeability transition. Nat Commun 10:688.

931 53. Tian N, Chu H, Li Q, Sun H, Zhang J, Chu N, Sun Z. 2025. Host-directed therapy for tuberculosis. Eur J
932 Med Res 30:267.

933 54. Buha I, Škodrić-Trifunović V, Adžić-Vukičević T, Ilić A, Blanka-Protić A, Stjepanovic M, Anđelković M,
934 Vreća M, Milin-Lazović J, Spasovski V, Pavlović S. 2019. Relevance of TNF-α, IL-6 and IRAK1 gene
935 expression for assessing disease severity and therapy effects in tuberculosis patients. J Infect Dev
936 Ctries 13:419–425.

937 55. Naicker N, Sigal A, Naidoo K. 2020. Metformin as Host-Directed Therapy for TB Treatment: Scoping
938 Review. Front Microbiol 11:435.

939 56. de Waal AM, Hiemstra PS, Ottenhoff TH, Joosten SA, van der Does AM. 2022. Lung epithelial cells
940 interact with immune cells and bacteria to shape the microenvironment in tuberculosis. Thorax
941 77:408–416.

942 57. Leon-Icaza SA, Bagayoko S, Vergé R, Iakobachvili N, Ferrand C, Aydogan T, Bernard C, Sanchez Dafun
943 A, Murris-Espin M, Mazières J, Bordignon PJ, Mazères S, Bernes-Lasserre P, Ramé V, Lagarde J-M,
944 Marcoux J, Bousquet M-P, Chalut C, Guilhot C, Clevers H, Peters PJ, Molle V, Lugo-Villarino G, Cam K,
945 Berry L, Meunier E, Cougoule C. 2023. Druggable redox pathways against Mycobacterium abscessus in
946 cystic fibrosis patient-derived airway organoids. PLoS Pathog 19:e1011559.

947 58. Agudelo CW, Samaha G, Garcia-Arcos I. 2020. Alveolar lipids in pulmonary disease. A review. Lipids
948 Health Dis 19:122.

949 59. Little I, Bersie S, Redente EF, McCubbrey AL, Tarling EJ. 2025. Alveolar macrophages: guardians of the
950 alveolar lipid galaxy. Curr Opin Lipidol 36:153–162.

951 60. Pisu D, Johnston L, Mattila JT, Russell DG. 2024. The frequency of CD38+ alveolar macrophages
952 correlates with early control of M. tuberculosis in the murine lung. Nat Commun 15:8522.

953 61. Pisu D, Huang L, Grenier JK, Russell DG. 2020. Dual RNA-Seq of Mtb-Infected Macrophages In Vivo
954 Reveals Ontologically Distinct Host-Pathogen Interactions. Cell Rep 30:335-350.e4.

955 62. Heifets L, Higgins M, Simon B. 2000. Pyrazinamide is not active against Mycobacterium tuberculosis
956 residing in cultured human monocyte-derived macrophages. Int J Tuberc Lung Dis Off J Int Union
957 Tuberc Lung Dis 4:491–495.

958 63. Malone L, Schurr A, Lindh H, McKENZIE D, Kiser JS, Williams JH. 1952. The effect of pyrazinamide
959 (aldinamide) on experimental tuberculosis in mice. Am Rev Tuberc 65:511–518.

960 64. McDermott W, Tompsett R. 1954. Activation of pyrazinamide and nicotinamide in acidic
961 environments in vitro. Am Rev Tuberc 70:748–754.

962 65. Solotorovsky M, Gregory FJ, Ironson EJ, Bugie EJ, O'neill RC, Pfister R. 1952. Pyrazinoic acid amide; an
963 agent active against experimental murine tuberculosis. Proc Soc Exp Biol Med Soc Exp Biol Med N Y N
964 79:563–565.

965 66. Tarshis MS, Weed WA. 1953. Lack of significant in vitro sensitivity of Mycobacterium tuberculosis to
966 pyrazinamide on three different solid media. Am Rev Tuberc 67:391–395.

967 67. Pisu D, Huang L, Narang V, Theriault M, Lê-Bury G, Lee B, Lakudzala AE, Mzinza DT, Mhango DV,
968 Mitini-Nkhoma SC, Jambo KC, Singhal A, Mwandumba HC, Russell DG. 2021. Single cell analysis of M.
969 tuberculosis phenotype and macrophage lineages in the infected lung. J Exp Med 218:e20210615.

970 68. Krug S, Parveen S, Bishai WR. 2021. Host-Directed Therapies: Modulating Inflammation to Treat
971 Tuberculosis. Front Immunol 12:660916.

972 69. Gries R, Sala C, Rybniker J. 2020. Host-Directed Therapies and Anti-Virulence Compounds to Address
973 Anti-Microbial Resistant Tuberculosis Infection. Appl Sci 10:2688.

974 70. Armesilla-Diaz A, Pilar Arenaz M, Ashby C, Blanco D, D'Oria E, Garuti H, Gómez V, González-Del-Río R,
975 Martínez-Hoyos M, Meiler E, Mendoza-Losana A, Mohamet L, Padrón-Barthe L, Pérez E, Pérez L,

976 Remuiñán MJ, Rodríguez-Miquel B, Segura-Carro D, Viera-Morilla S. 2025. High-throughput screening
977 of small molecules targeting Mycobacterium tuberculosis in human iPSC macrophages. Antimicrob
978 Agents Chemother 69:e0161324.

979 71. Roth D, Şahin AT, Ling F, Tepho N, Senger CN, Quiroz EJ, Calvert BA, van der Does AM, Güney TG, Glasl
980 S, van Schadewijk A, von Schledorn L, Olmer R, Kanso E, Nawroth JC, Ryan AL. 2025. Structure and
981 function relationships of mucociliary clearance in human and rat airways. Nat Commun 16:2446.

982 72. Beckwith KS, Beckwith MS, Ullmann S, Sætra RS, Kim H, Marstad A, Åsberg SE, Strand TA, Haug M,
983 Niederweis M, Stenmark HA, Flo TH. 2020. Plasma membrane damage causes NLRP3 activation and
984 pyroptosis during Mycobacterium tuberculosis infection. Nat Commun 11:2270.

985 73. Bomfim CCB, Fisher L, Amaral EP, Mittereder L, McCann K, Correa AAS, Namasivayam S, Swamydas M,
986 Moayeri M, Weiss JM, Chari R, McVicar DW, Costa DL, D'Império Lima MR, Sher A. 2022.
987 Mycobacterium tuberculosis Induces Irg1 in Murine Macrophages by a Pathway Involving Both TLR-2
988 and STING/IFNAR Signaling and Requiring Bacterial Phagocytosis. Front Cell Infect Microbiol
989 12:862582.

990 74. Bullen CK, Singh AK, Krug S, Lun S, Thakur P, Srikrishna G, Bishai WR. 2023. MDA5 RNA-sensing
991 pathway activation by Mycobacterium tuberculosis promotes innate immune subversion and
992 pathogen survival. JCI Insight 8:e166242.

993 75. Saiga H, Kitada S, Shimada Y, Kamiyama N, Okuyama M, Makino M, Yamamoto M, Takeda K. 2012.
994 Critical role of AIM2 in Mycobacterium tuberculosis infection. Int Immunol 24:637–644.

995 76. Wassermann R, Gulen MF, Sala C, Perin SG, Lou Y, Rybniker J, Schmid-Burgk JL, Schmidt T, Hornung V,
996 Cole ST, Ablasser A. 2015. Mycobacterium tuberculosis Differentially Activates cGAS- and
997 Inflammasome-Dependent Intracellular Immune Responses through ESX-1. Cell Host Microbe 17:799–
998 810.

999 77. Bafica A, Scanga CA, Feng CG, Leifer C, Cheever A, Sher A. 2005. TLR9 regulates Th1 responses and
1000 cooperates with TLR2 in mediating optimal resistance to Mycobacterium tuberculosis. J Exp Med
1001 202:1715–1724.

1002 78. Shukla S, Richardson ET, Drage MG, Boom WH, Harding CV. 2018. Mycobacterium tuberculosis
1003 Lipoprotein and Lipoglycan Binding to Toll-Like Receptor 2 Correlates with Agonist Activity and
1004 Functional Outcomes. Infect Immun 86:e00450-18.

1005 79. Olson GS, Murray TA, Jahn AN, Mai D, Diercks AH, Gold ES, Aderem A. 2021. Type I interferon
1006 decreases macrophage energy metabolism during mycobacterial infection. Cell Rep 35:109195.

1007 80. Scriba TJ, Maseeme M, Young C, Taylor L, Leslie AJ. 2024. Immunopathology in human tuberculosis.
1008 Sci Immunol 9:eado5951.

1009 81. Winder FG, Collins P, Rooney SA. 1970. Effects of isoniazid on mycolic acid synthesis in
1010 Mycobacterium tuberculosis and on its cell envelope. Biochem J 117:27P.

1011 82. Timmins GS, Deretic V. 2006. Mechanisms of action of isoniazid. Mol Microbiol 62:1220–1227.

1012 83. Naidoo A, Naidoo K, McIlleron H, Essack S, Padayatchi N. 2017. A review of moxifloxacin for the
1013 treatment of drug-susceptible tuberculosis. J Clin Pharmacol 57:1369–1386.

1014 84. Guan Y, Liu Y. 2020. Meta-analysis on Effectiveness and Safety of Moxifloxacin in Treatment of
1015 Multidrug Resistant Tuberculosis in Adults. Medicine (Baltimore) 99:e20648.

1016 85. Zhang Y, Shi W, Zhang W, Mitchison D. 2014. Mechanisms of Pyrazinamide Action and Resistance.
1017 Microbiol Spectr 2:MGM2-0023–2013.

1018 86. Santucci P, Aylan B, Botella L, Bernard EM, Bussi C, Pellegrino E, Athanasiadi N, Gutierrez MG. 2022.
1019 Visualizing Pyrazinamide Action by Live Single-Cell Imaging of Phagosome Acidification and
1020 Mycobacterium tuberculosis pH Homeostasis. mBio 13:e0011722.

1021 87. Laudouze J, Rokitskaya TI, Abolet A, Point V, Firsov AM, Khailova LS, Cavalier J-F, Canaan S, Baulard
1022 AR, Antonenko YN, Gouzy A, Santucci P. 2025. Pyrazinamide kills Mycobacterium tuberculosis via pH-
1023 driven weak-acid permeation and cytosolic acidification. bioRxiv 2025.09.26.678883.

1024 88. Wehrli W. 1983. Rifampin: mechanisms of action and resistance. Rev Infect Dis 5 Suppl 3:S407-411.

1025 89. Telenti A, Imboden P, Marchesi F, Lowrie D, Cole S, Colston MJ, Matter L, Schopfer K, Bodmer T. 1993.
1026 Detection of rifampicin-resistance mutations in Mycobacterium tuberculosis. Lancet Lond Engl
1027 341:647–650.

1028 90. Gan WC, Ng HF, Ngeow YF. 2023. Mechanisms of Linezolid Resistance in Mycobacteria.
1029 Pharmaceuticals 16:784.

1030 91. Dietze R, Hadad DJ, McGee B, Molino LPD, Maciel ELN, Peloquin CA, Johnson DF, Debanne SM,
1031 Eisenach K, Boom WH, Palaci M, Johnson JL. 2008. Early and extended early bactericidal activity of
1032 linezolid in pulmonary tuberculosis. Am J Respir Crit Care Med 178:1180–1185.

1033 92. Ivanyi J, Zumla A. 2013. Nonsteroidal antiinflammatory drugs for adjunctive tuberculosis treatment. J
1034 Infect Dis 208:185–188.

1035 93. Cubillos-Angulo JM, Nogueira BMF, Arriaga MB, Barreto-Duarte B, Araújo-Pereira M, Fernandes CD,
1036 Vinhaes CL, Villalva-Serra K, Nunes VM, Miguez-Pinto JP, Amaral EP, Andrade BB. 2022. Host-directed
1037 therapies in pulmonary tuberculosis: Updates on anti-inflammatory drugs. Front Med 9:970408.

1038 94. Hölscher C, Gräb J, Hölscher A, Müller AL, Schäfer SC, Rybniker J. 2020. Chemical p38 MAP kinase
1039 inhibition constrains tissue inflammation and improves antibiotic activity in Mycobacterium
1040 tuberculosis-infected mice. Sci Rep 10:13629.

1041 95. Guerra-De-Blas PDC, Torres-González P, Bobadilla-Del-Valle M, Sada-Ovalle I, Ponce-De-León-Garduño
1042 A, Sifuentes-Osornio J. 2018. Potential Effect of Statins on Mycobacterium tuberculosis Infection. J
1043 Immunol Res 2018:7617023.

1044 96. Guerra-De-Blas PDC, Bobadilla-Del-Valle M, Sada-Ovalle I, Estrada-García I, Torres-González P, López-
1045 Saavedra A, Guzmán-Beltrán S, Ponce-de-León A, Sifuentes-Osornio J. 2019. Simvastatin Enhances the
1046 Immune Response Against Mycobacterium tuberculosis. Front Microbiol 10:2097.

1047 97. Parihar SP, Guler R, Khutlang R, Lang DM, Hurdayal R, Mhlanga MM, Suzuki H, Marais AD, Brombacher
1048 F. 2014. Statin therapy reduces the mycobacterium tuberculosis burden in human macrophages and
1049 in mice by enhancing autophagy and phagosome maturation. J Infect Dis 209:754–763.

1050 98. Singhal A, Jie L, Kumar P, Hong GS, Leow MK-S, Paleja B, Tsenova L, Kurepina N, Chen J, Zolezzi F,
1051 Kreiswirth B, Poidinger M, Chee C, Kaplan G, Wang YT, De Libero G. 2014. Metformin as adjunct
1052 antituberculosis therapy. Sci Transl Med 6:263ra159.

1053 99. Johnson BK, Colvin CJ, Needle DB, Mba Medie F, Champion PAD, Abramovitch RB. 2015. The Carbonic
1054 Anhydrase Inhibitor Ethoxzolamide Inhibits the Mycobacterium tuberculosis PhoPR Regulon and Esx-1
1055 Secretion and Attenuates Virulence. Antimicrob Agents Chemother 59:4436–4445.

1056 100. Rybniker J, Chen JM, Sala C, Hartkoorn RC, Vocat A, Benjak A, Boy-Röttger S, Zhang M, Székely R, Greff
1057 Z, Orfi L, Szabadkai I, Pató J, Kéri G, Cole ST. 2014. Anticytolytic screen identifies inhibitors of
1058 mycobacterial virulence protein secretion. Cell Host Microbe 16:538–548.

1059

1060

9. FIGURE LEGENDS

Figure 1. Phenotypic Characterization of the human AML cell model reproduces the anti-inflammatory and immunoregulatory phenotype of hAMs. A) Schematic illustration of alveolar macrophage-like cells (AML) generation from peripheral $CD14^+$ monocytes (created with BioRender.com). **B)** Flow cytometry dot plots showing the expression of CD206 vs. CD64 and CD16 vs. CD14 in human alveolar macrophages (hAMs) recovered from bronchoalveolar lavage (BAL) and AMLs, and corresponding quantification of the indicated cell subsets. **C)** Graphs showing the median fluorescence intensity (MFI) of different markers in the $CD206^+CD64^+CD14^+CD16^+$ subpopulation of hAMs (left) and the corresponding subpopulation of AMLs (right). In the graphs, each dot represents an individual donor. Significant differences were determined using an unpaired, non-parametric Kruskal–Wallis test. $p < 0.05$ (*), $p < 0.01$ (**), $p < 0.001$ (***).

Figure 2. Mtb infection induces a phenotypic heterogeneity within the AML compartment. AML cells were infected *in vitro* with H37Rv-GFP (MOI 1:1) for 4h, washed, and then incubated for 6 days. **A)** AML uninfected and Mtb-infected were visualized using transmission electron microscopy (TEM). Bacteria are shown in magenta. Scale bars: 2 µm. LB (lipid body) ; PhL (phagolysosome) ; M (mitochondria) ; sRE (smooth endoplasmic reticulum). **B)** Relative gene expression of *PPARG*, *SPI1* (PU.1), *MMP7*, *MMP9*, *TNF,* and *IL10* in control (uninfected) and Mtb-infected AML cells assessed by RT-qPCR. **C)** Flow cytometry dot plots and graphs showing the frequency of $CD14^+CD16^-$, and $CD14^+CD16^+$ subpopulations in control (uninfected) and Mtb-infected AML cells. **D)** Flow cytometry histogram and graph showing the median fluorescence intensity (MFI) of Mtb in $CD14^+CD16^-$, and $CD14^+CD16^+$ subpopulations among Mtb-infected AML cells. **E)** Unsupervised t-SNE analysis of flow cytometry data from control (uninfected) and Mtb-infected AMLs, stratified by CD16 expression. Histograms show the MFI of different markers analyzed in $CD16^+$ and $CD16^-$ subpopulations. **F)** Histograms and graphs showing the median fluorescence intensity (MFI) of CD86, CD163, CD169, CD209, and MARCO in $CD14^+CD16^+$ and $CD14^+CD16^-$ AML subpopulations in control (uninfected) and Mtb-infected AML cells. **G)** Relative gene expression of *IFNA*, *IFNB*, *MX1*, *MX2*, *ISG15,* and *SIGLEC1* in control (uninfected) and Mtb-infected AML cells assessed by RT-qPCR. In the graphs, each dot represents an individual donor. Significant differences were determined using a paired, non-parametric Wilcoxon test. $p < 0.05$ (*), $p < 0.01$ (**), $p < 0.001$ (***).

Figure 3. Transcriptomic response of primary hAM to Mtb infection. Gene expression levels of primary hAM derived from different healthy donors and infected *ex vivo* with H37Rv for 72h were analyzed using publicly available RNA-seq datasets. **A)** Heatmap of selected differentially expressed genes between AML, hAM, and MDM cellular models. Red indicates upregulated genes and blue indicates downregulated genes. Genes showing significant differences between AML and MDM (adjusted $p < 0.05$) are marked with an asterisk (*). **B)** Volcano plot highlighting the top 40 DEGs (fold change ≥ ±1.5; adjusted $p < 0.05$). Red dots indicate upregulated genes, blue dots indicate downregulated genes, and grey dots represent genes outside the threshold. **C)** Reactome pathway enrichment analysis of upregulated genes in 72 h Mtb-infected hAMs compared with uninfected controls. Dot size reflects the number of genes per pathway, and color corresponds to the adjusted *p*-value.

1103 **Figure 4. Evaluation of Bacterial Control and Host Response Modulation by Anti-TB Agents in**
1104 **AML cells.** AMLs were infected with H37Rv::lux at an MOI of 1:1 for 4h, washed, and then treated
1105 with different compounds (SoC= standard-of-care antibiotics; VTT= virulence-targeting therapies;
1106 HDT=host-directed therapies), and incubated for 6 days. **A)** Heatmap showing luminescence
1107 inhibition. **B)** Colony-forming unit (CFU) of Mtb-infected AML cells. **C)** TNF-α and IL-6 production by
1108 Mtb-infected AML cells. In the graphs, each dot represents an individual donor. Significant
1109 differences were determined using an unpaired, non-parametric Mann–Whitney test. $p < 0.05$ (**), $p < 0.01$ (**), $p < 0.001$ (***).
1110
1111

1112 **Figure 5. Airway ALI cultures recapitulate the human pulmonary environment and support Mtb**
1113 **infection.** Human airway organoid/ALI cultures were derived from tumor-adjacent normal lung
1114 tissue obtained from different patients. For infection experiments (panels H–J), differentiated
1115 airway ALI cultures were infected with H37Rv::lux (4×10^5 bacilli/insert) on the apical side and
1116 incubated for 6 days. **A)** Schematic illustration of airway ALI culture generation from lung biopsy
1117 (created with BioRender.com). **B)** Airway ALI cultures visualized using light microscopy. Scale bars:
1118 650µm or 75 µm. **C)** Hematoxylin & Eosin (H&E) staining on an airway ALI cross-section. Scale bars:
1119 50 µm. **D)** Alcian blue staining of airway ALI cross-section. Scale bars: 50 µm. **E)** Scanning electron
1120 microscopy (SEM) of airway ALI cultures showing a differentiated bronchial epithelium. Red arrows
1121 indicate cilia, asterisks indicate goblet cells, and yellow arrows indicate microvilli. Scale bars: 20µm
1122 or 5µm. **F)** Dextran flux assay showing permeability defined by apical-to-basolateral flux (Papp) of
1123 TRITC-dextran 4 kDa or FITC-dextran 70 kDa. **G)** Transepithelial electrical resistance measurement
1124 of airway ALI cultures. **H)** Luminescence and CFUs measured in the apical compartment at day 0 and
1125 day 6 post-infection (p.i.). **I)** Measurement of luminescence and CFUs at apical and basal
1126 compartments at days 6 p.i. **J)** Scanning electron microscopy (SEM) image of Mtb-infected airway
1127 ALI cultures. Scale bar: 100µm or 5µM. Significant differences were determined using an unpaired,
1128 non-parametric Mann–Whitney test. $p < 0.05$ (**), $p < 0.01$ (**), $p < 0.001$ (***).
1129

1130 **Figure 6. Evaluation of Bacterial Control and Host Response Modulation by Anti-TB Agents in**
1131 **Human Airway Air–Liquid Interface (ALI) System.** Airway ALI cultures were infected with H37Rv::lux
1132 (400.000 bac/insert) at the apical side, treated with different compounds (SoC= standard-of-care
1133 antibiotics; VTT= virulence-targeting therapies; HDT=host-directed therapies) in the basal
1134 compartment, and incubated for 6 days. **A)** Heatmap showing luminescence inhibition. **B)** Colony-
1135 forming unit (CFU) of Mtb-infected airway ALI model. **C)** IL-6 and IL-8 production by the Mtb-infected
1136 airway ALI model. Significant differences were determined using an unpaired, non-parametric
1137 Mann–Whitney test. $p < 0.05$ (**), $p < 0.01$ (**), $p < 0.001$ (***).

Figure 1

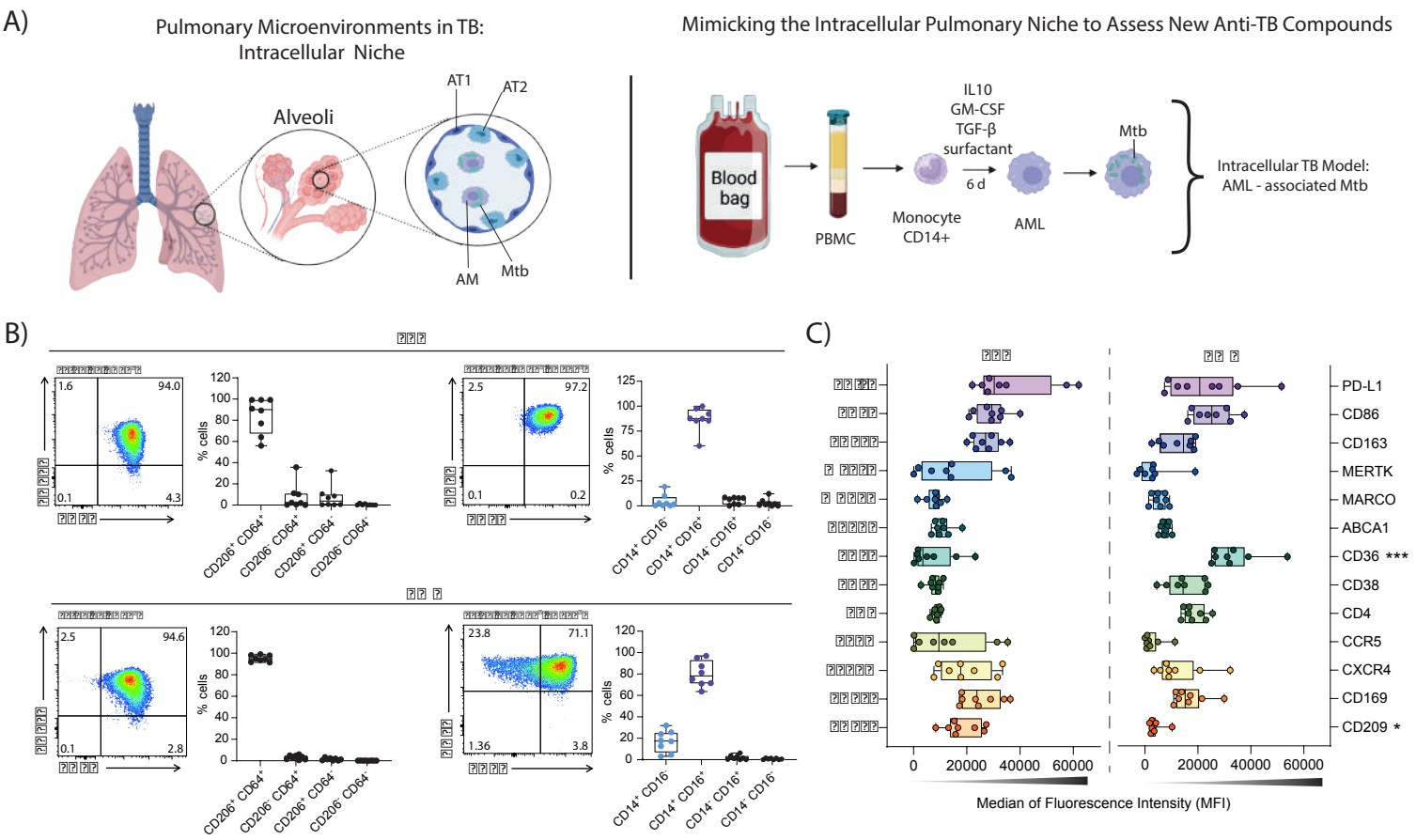
A)
Pulmonary Microenvironments in TB:
Intracellular Niche
Alveoli
AT1
AT2
AM
Mtb
Mimicking the Intracellular Pulmonary Niche to Assess New Anti-TB Compounds
Blood bag
PBMC
IL10
GM-CSF
TGF-β
surfactant
6 d
Monocyte CD14+
AML
Mtb
Intracellular TB Model:
AML - associated Mtb
B)
% cells
CD206+ CD64+
CD206- CD64+
CD206+ CD64-
CD206- CD64-
CD14+ CD16-
CD14+ CD16+
CD14- CD16+
CD14- CD16-
C)
PD-L1
CD86
CD163
MERTK
MARCO
ABCA1
CD36 ***
CD38
CD4
CCR5
CXCR4
CD169
CD209 *
Median of Fluorescence Intensity (MFI)

Figure 2

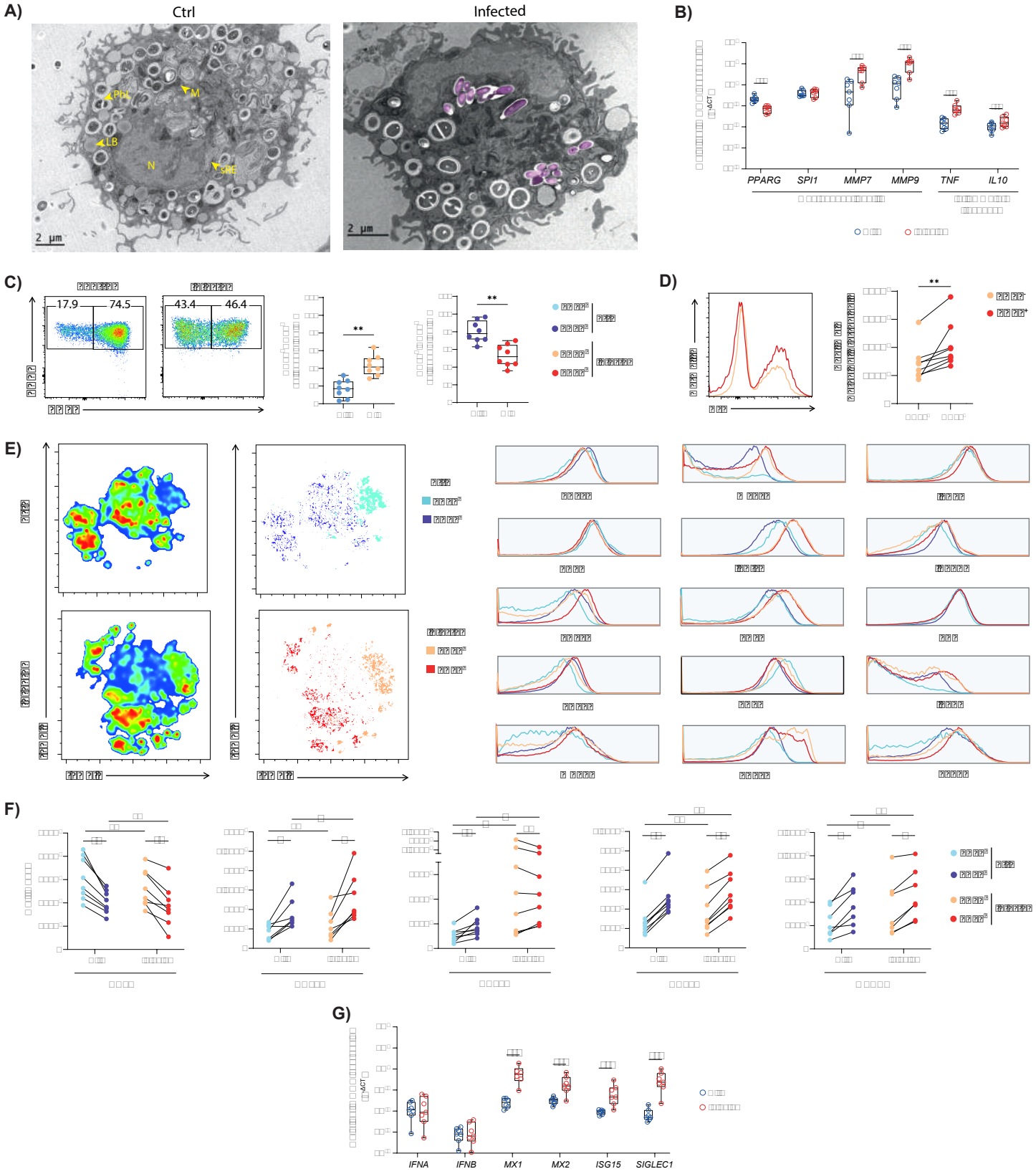
A)
Ctrl
Infected
Pbx
M
LB
N
CRE
2 µm
2 µm
B)
PPARG
SPI1
MMP7
MMP9
TNF
IL10
C)
17.9
74.5
43.4
46.4
**
**
D)
**
E)
F)
G)
IFNA
IFNB
MX1
MX2
ISG15
SIGLEC1

Figure 3

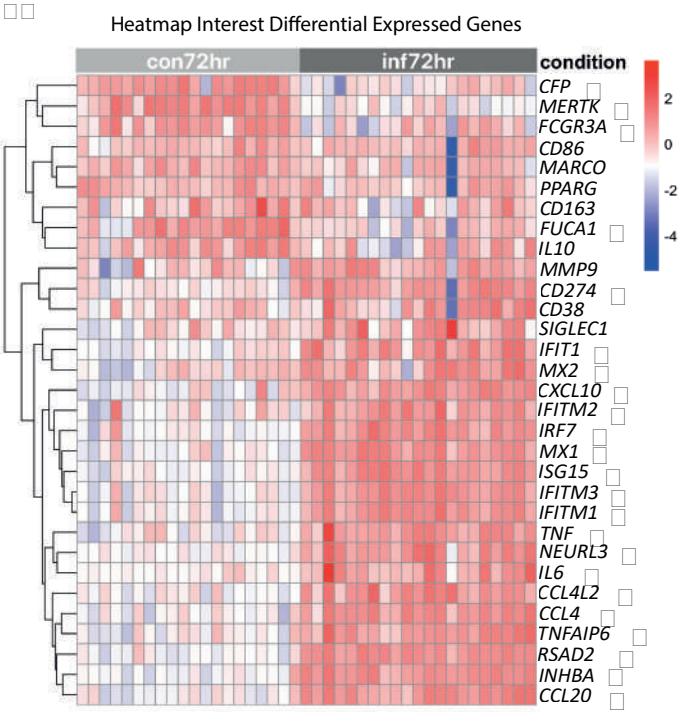
Heatmap Interest Differential Expressed Genes
con72hr
inf72hr
condition
CFP
MERTK
FCGR3A
CD86
MARCO
PPARG
CD163
FUCA1
IL10
MMP9
CD274
CD38
SIGLEC1
IFIT1
MX2
CXCL10
IFITM2
IRF7
MX1
ISG15
IFITM3
IFITM1
TNF
NEURL3
IL6
CCL4L2
CCL4
TNFAIP6
RSAD2
INHBA
CCL20
2
0
-2
-4

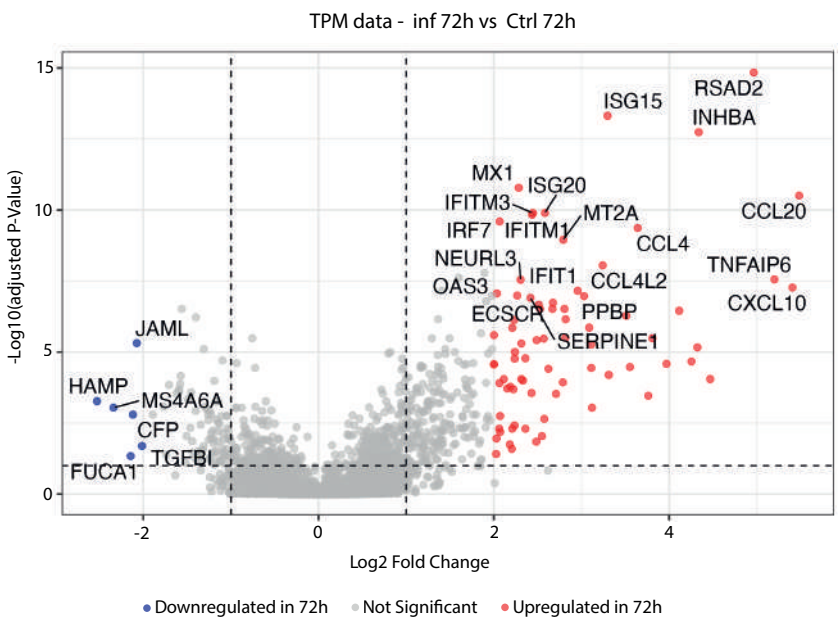
TPM data - inf 72h vs Ctrl 72h
-Log10(adjusted P-Value)
Log2 Fold Change
ISG15
RSAD2
INHBA
MX1
ISG20
IFITM3
MT2A
CCL20
IRF7
IFITM1
CCL4
NEURL3
TNFAIP6
OAS3
IFIT1
CCL4L2
CXCL10
ECSCR
PPBP
SERPINE1
JAML
HAMP
MS4A6A
CFP
TGFBL
FUCA1
Downregulated in 72h
Not Significant
Upregulated in 72h

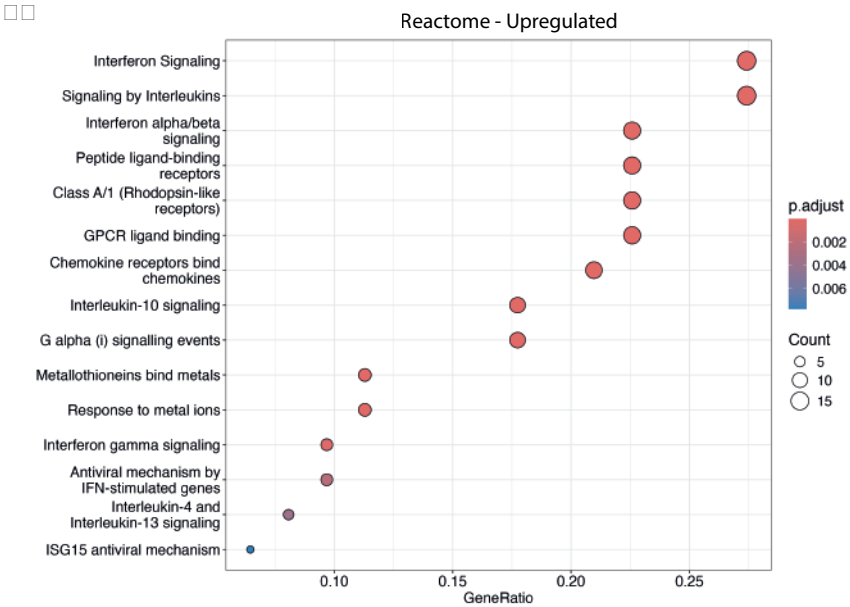
Reactome - Upregulated
Interferon Signaling
Signaling by Interleukins
Interferon alpha/beta signaling
Peptide ligand-binding receptors
Class A/1 (Rhodopsin-like receptors)
GPCR ligand binding
Chemokine receptors bind chemokines
Interleukin-10 signaling
G alpha (i) signalling events
Metallothioneins bind metals
Response to metal ions
Interferon gamma signaling
Antiviral mechanism by IFN-stimulated genes
Interleukin-4 and Interleukin-13 signaling
ISG15 antiviral mechanism
GeneRatio
p.adjust
0.002
0.004
0.006
Count
5
10
15

Figure 4

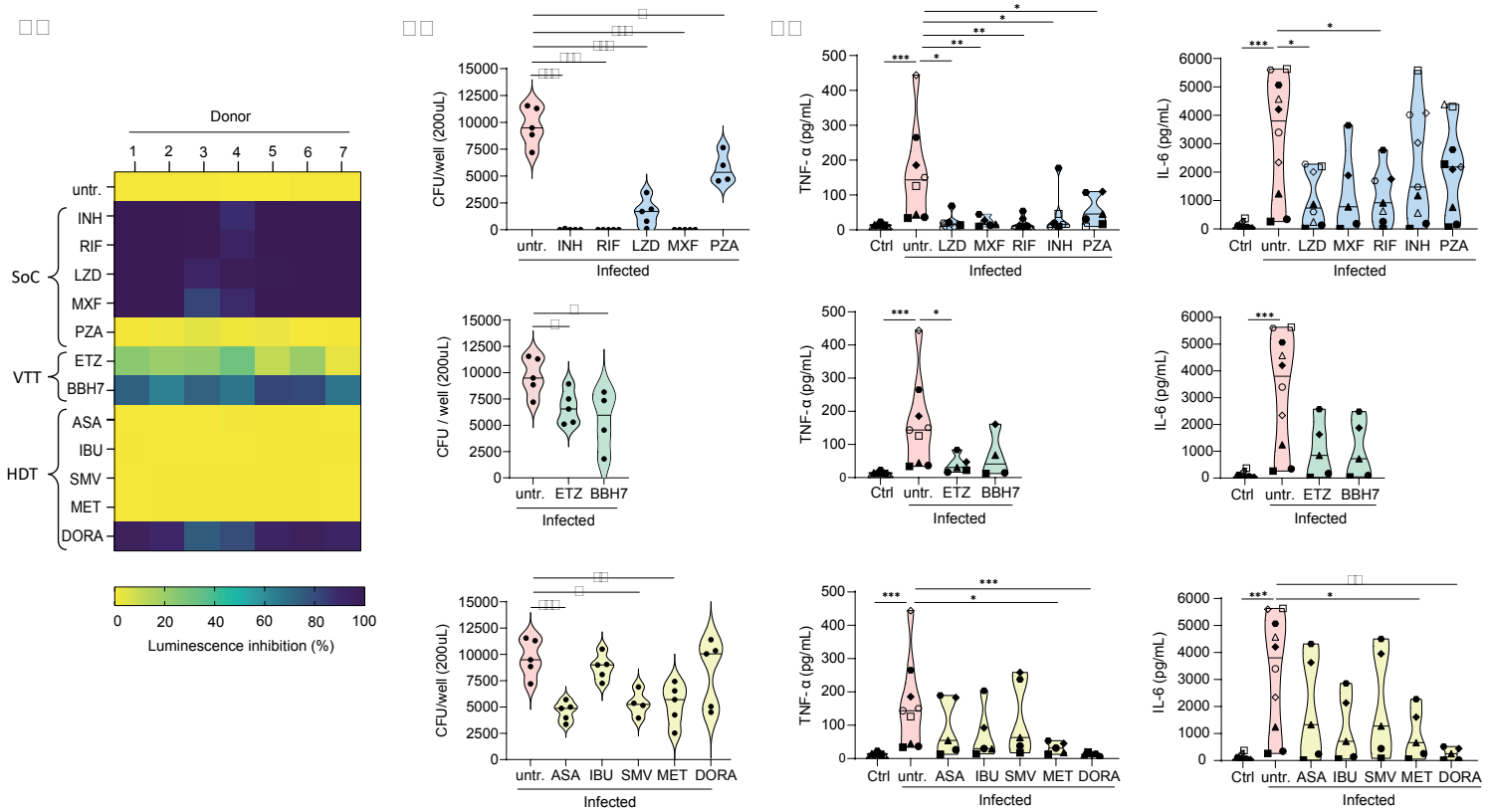
Donor
1 2 3 4 5 6 7
untr.
INH
RIF
LZD
MXF
PZA
SoC
ETZ
BBH7
VTT
ASA
IBU
SMV
MET
DORA
HDT
0 20 40 60 80 100
Luminescence inhibition (%)
CFU/well (200uL)
CFU / well (200uL)
untr. INH RIF LZD MXF PZA
untr. ETZ BBH7
untr. ASA IBU SMV MET DORA
Infected
TNF- α (pg/mL)
Ctrl untr. LZD MXF RIF INH PZA
Ctrl untr. ETZ BBH7
Ctrl untr. ASA IBU SMV MET DORA
IL-6 (pg/mL)

Figure 5

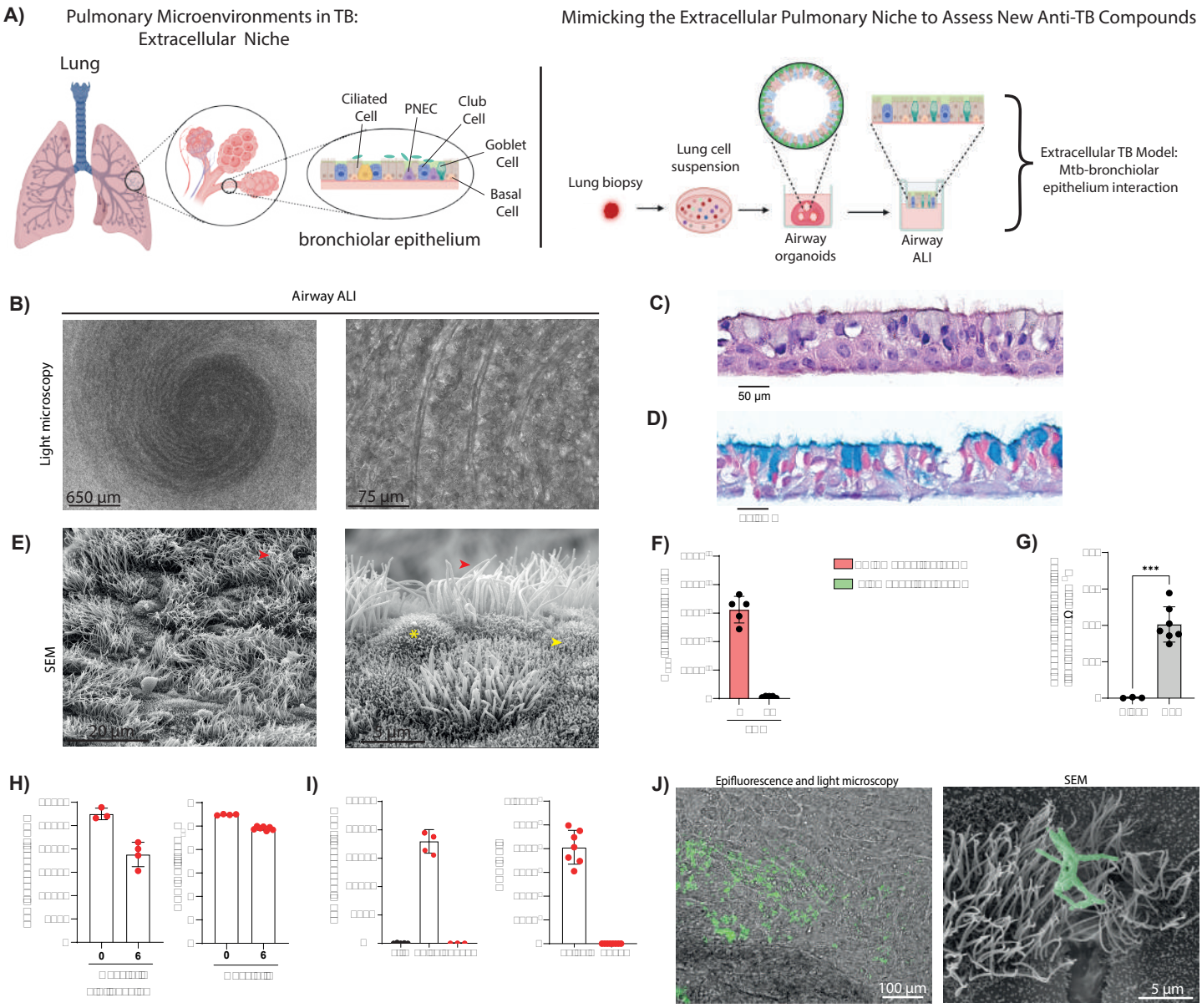
A)
Pulmonary Microenvironments in TB:
Extracellular Niche
Lung
Ciliated Cell
PNEC
Club Cell
Goblet Cell
Basal Cell
bronchiolar epithelium
Mimicking the Extracellular Pulmonary Niche to Assess New Anti-TB Compounds
Lung biopsy
Lung cell suspension
Airway organoids
Airway ALI
Extracellular TB Model:
Mtb-bronchiolar epithelium interaction
B)
Airway ALI
Light microscopy
650 µm
75 µm
C)
50 µm
D)
E)
SEM
20 µm
5 µm
F)
G)
***
H)
0
6
I)
J)
Epifluorescence and light microscopy
SEM
100 µm
5 µm

Figure 6

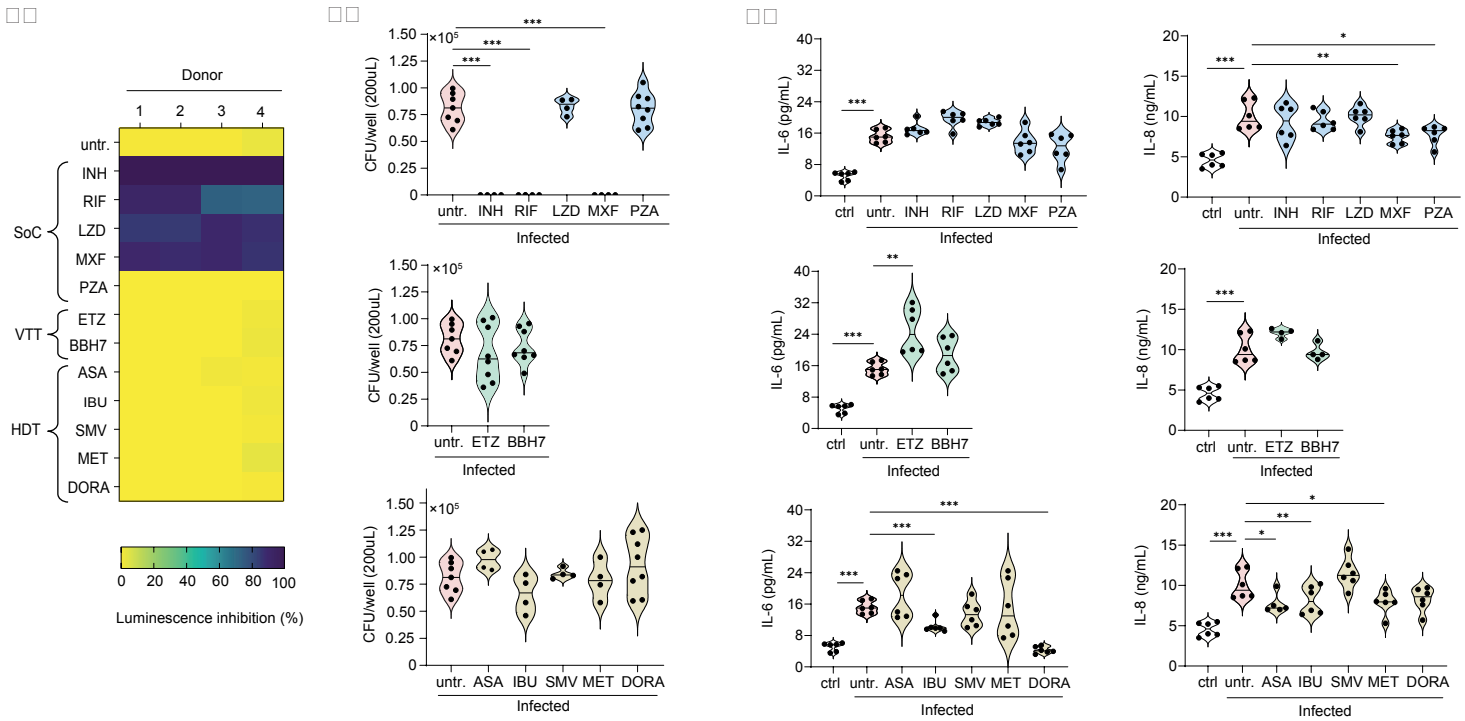
Donor
1 2 3 4
untr.
INH
RIF
LZD
MXF
PZA
SoC
ETZ
BBH7
VTT
ASA
IBU
SMV
MET
DORA
HDT
0 20 40 60 80 100
Luminescence inhibition (%)
CFU/well (200uL)
×10^5
untr. INH RIF LZD MXF PZA
untr. ETZ BBH7
untr. ASA IBU SMV MET DORA
Infected
IL-6 (pg/mL)
IL-8 (ng/mL)
ctrl
***
**
*